Large-scale conformational changes of FhaC provide insights into the two-partner secretion mechanism

G. Sicoli[1*], A. Konijnenberg[2*$], J. Guerin[3$], S. Hessmann[4,5], E. Del Nero[4,5], O. Hernandez-Alba[4,5], S. Lecher[3], G. Rouaut[6], L. Müggenburg[6$], H. Vezin[1], S. Cianférani[4,5], F. Sobott[2,7], R. Schneider[6$£], F. Jacob-Dubuisson[3£]

[1] Laboratoire Avancé de Spectroscopie pour les Interactions, la Réactivité et l'Environnement (LASIRE), UMR CNRS 8516, Université de Lille, Avenue Paul Langevin – C4, F-59655 Villeneuve d'Ascq Cedex, France

[2] BAMS Research group, University of Antwerp, Groenenborgerlaan 171, 2020 Antwerp, Belgium

[3] CNRS, INSERM, Institut Pasteur de Lille, U1019-UMR9017-CIIL-Center for Infection and Immunity of Lille, F-59000, Lille, France

[4] Laboratoire de Spectrométrie de Masse BioOrganique, Université de Strasbourg, CNRS, IPHC UMR 7178, Strasbourg 67000, France

[5] Infrastructure Nationale de Protéomique ProFI – FR2048, 67087 Strasbourg, France

[6] ERL 9002 CNRS Biologie Structurale Intégrative, UMR INSERM 1167, Université de Lille, 50 Avenue Halley, F-59650 Villeneuve d'Ascq, France

[7] Astbury Centre for Structural Molecular Biology and the School of Molecular and Cellular Biology, University of Leeds, Leeds LS2 9JT, United Kingdom

[*] These authors contributed equally.

[£] These authors contributed equally. For correspondence: robert.schneider@univ-lille.fr;

francoise.jacob@ibl.cnrs.fr

[$] current addresses: AK, Thermo Fisher Scientific, Zwaanstraat 31 G/H, Building TR, 5651 Eindhoven, The Netherlands; JG, Calixar, 60 avenue Rockefeller, 69008 Lyon, France; LM, Institut für Organische Chemie, Gottfried Wilhelm Leibniz Universität Hannover, Schneiderberg 1B, DE-30167 Hannover, Germany; RS, Bruker Switzerland AG, Industriestrasse 26, CH-8117 Fällanden, Switzerland.

Abstract

The Two-Partner secretion pathway mediates protein transport across the outer membrane of Gram-negative bacteria. TpsB transporters belong to the Omp85 superfamily, whose members catalyze protein insertion into, or translocation across membranes without external energy sources. They are composed of a transmembrane β barrel preceded by two periplasmic POTRA domains that bind the incoming protein substrate. Here we used an integrative approach combining *in vivo* assays, mass spectrometry, nuclear magnetic resonance and electron paramagnetic resonance techniques suitable to detect minor states in heterogeneous populations, to explore transient conformers of the TspB transporter FhaC. This revealed substantial, spontaneous conformational changes with a portion of the POTRA2 domain coming close to the lipid bilayer and surface loops. Specifically, the amphipathic β hairpin immediately preceding the first barrel strand can insert into the β barrel. We propose that these motions enlarge the channel and may hoist the substrate into it for secretion. An anchor region at the interface of the β barrel and the POTRA2 domain stabilizes the transporter in the course of secretion. Our data propose a solution to the conundrum how these proteins mediate protein secretion without the need for cofactors, by utilizing intrinsic protein dynamics.

Introduction

The Two-Partner Secretion (TPS) pathway is dedicated to the export of large proteins notably serving as virulence factors (Guerin et al., 2017). The TpsB transporters are transmembrane β-barrel proteins that secrete their substrates, collectively called TpsA proteins, across the outer membrane of various Gram-negative bacteria. They belong to the ubiquitous Omp85 superfamily whose members mediate protein insertion into, or translocation across membranes of bacteria and

2

51 eukaryotic organelles, and which includes the essential bacterial BamA transporters (Heinz &

52 Lithgow, 2014; Knowles et al., 2009; Noinaj et al., 2017). The FhaB/FhaC pair of *Bordetella*

53 *pertussis* is a model TPS system, in which the FhaC transporter mediates the translocation of the

54 adhesin FhaB across the outer membrane (Fan et al., 2012).

55   Omp85 transporters are composed of N-terminal POTRA domains - two in the case of TpsB

56 transporters - followed by a 16-stranded transmembrane β barrel, which for FhaC is the FhaB

57 translocation pore (Baud et al., 2014). The POTRA domains mediate protein-protein interactions

58 in the periplasm, and notably recognition of client proteins (Delattre et al., 2011). Another

59 hallmark feature of the Omp85 superfamily is the extracellular loop L6 that folds back inside the

60 barrel and harbors a conserved motif at its tip forming a salt bridge interaction with a specific motif

61 of the inner β-barrel wall (Gu et al., 2016; Maier et al., 2015; Noinaj et al., 2013).

62   A specific feature of TpsB transporters is an N-terminal α helix called H1 that plugs the β barrel

63 (Clantin et al., 2007; Guerin et al., 2014; Guerin et al., 2020; Maier et al., 2015). An extended

64 linker follows H1 and joins it to the POTRA1 domain in the periplasm. Recently, the X-ray

65 structures of other TpsB transporters, CdiB[Ab] and CdiB[Ec], have shown very similar folds to that of

66 FhaC, albeit with slightly different positions of H1 in the barrel (Guerin et al., 2020). Both H1 and

67 L6 stabilize the barrel in a closed conformation that most likely corresponds to the resting state of

68 the transporter (Guerin et al., 2020; Maier et al., 2015). The β barrel, the L6 loop and the two

69 POTRA domains are essential for transport activity (Clantin et al., 2007).

70   Omp85 transporters likely function in the absence of ATP or an electrochemical gradient. They

71 appear to be very dynamic and to undergo conformational cycling (Doerner & Sousa, 2017; Guerin

72 et al., 2020; Hartmann et al., 2018; Iadanza et al., 2020; Renault et al., 2011; Warner et al., 2017).

73 Lateral opening of the barrel between the first and last anti-parallel β strands is a common

74 mechanistic feature of Omp85 transporters, which is involved in their respective functions

75 (Diederichs et al., 2020; Doyle & Bernstein, 2019; Estrada Mallarino et al., 2015; Guerin et al.,

76 2020; Höhr et al., 2018; Iadanza et al., 2016; Noinaj et al., 2014; Tomasek et al., 2020).

77 The mechanism of two-partner secretion remains poorly understood, but it is known to involve

78 substantial conformational changes of the transporter including exit of H1 from the β barrel and

79 motions of the L6 loop (Guerin et al., 2014; Guerin et al., 2020; Guerin et al., 2015). The motion

80 of H1 toward the periplasm is facilitated by conformational changes of flexible regions of the

81 barrel, in particular the first β-barrel strand B1 and the extracellular loops L1, L2 and L6 (Guerin

82 et al., 2020). Binding of the N-terminal so-called TPS domain of the substrate protein to the

83 POTRA domains of its transporter also appears to enhance conformational changes (Guerin et al.,

84 2020; Guerin et al., 2015). How the substrate enters the pore and is progressively hoisted towards

85 the cell surface without backsliding to the periplasm remains unknown, but we hypothesize a cyclic

86 mechanism implying yet uncharacterized, transient conformations of TpsB transporters. In this

87 work we have explored such FhaC conformers using biophysical techniques suitable to detect

88 minor states in heterogeneous populations. Our data show that alternative conformational states of

89 FhaC exist even in the absence of its substrate and indicate that they are linked to its activity.

90

91 **Results**

92 **Effects of freezing the conformation of the POTRA2 domain on secretion activity**

93 To determine the importance of flexibility of the POTRA2 domain for FhaC function, we searched

94 for specific H bond- or salt bridge-mediated interactions present in the resting conformation (i.e.,

95 corresponding to the crystallographic structure) and disrupted them to loosen the structure or

96 conversely replaced them with disulfide (S-S) bonds to limit motions of the corresponding regions.

97   Of note, FhaC is naturally devoid of Cys residues. Residues involved in interactions between the

98   POTRA2 domain and the barrel (Asn^{245}-Ser^{157} and Asn^{245}-Lys^{184}) and in a barrel-distal region of

99   the POTRA2 domain (Asp^{165}-Lys^{171}) were replaced with Ala or Cys, and the effects of these

100   mutations on secretion activity were determined (Figure 1A-E). S-S bond formation is catalyzed

101   by the periplasmic disulfide oxidase DsbA in the course of biogenesis, which generally affects

102   SDS-PAGE migration of the protein in the absence of a reducing agent, unless the intervening

103   loop between the Cys residues is too short. The Asn^{245}Ala substitution markedly decreased the

104   activity of FhaC and somewhat reduced its amount in the membrane, unlike formation of Cys^{157}-

105   Cys^{245} or Cys^{184}-Cys^{245} S-S bonds (Figure 1C-E). This indicates that these barrel-POTRA2

106   interactions contribute to FhaC activity, possibly because they stabilize its conformation in the

107   secretion cycle. To the contrary, the engineered Cys^{165}+Cys^{171} substitutions strongly reduced the

108   level and the activity of FhaC in a $dsbA^+$ background. Although protein migration was not affected

109   the S-S bond was most likely formed, since secretion was not reduced in a $dsbA^-$ background or

110   with the individual substitutions. The observation that S-S bond formation between these two Cys

111   residues is detrimental points to the need for flexibility in this barrel-distal region of the POTRA2

112   domain.

113

114   **Spontaneous in vivo conformational changes of FhaC independent of substrate**

115   We simultaneously replaced two residues distant in the X-ray structure of FhaC with Cys residues

116   in order to detect alternative conformers of the transporter. The rationale was that conformational

117   changes of FhaC might promote spontaneous S-S bond formation if the two Cys residues come

118   close to each other, which might be detected even for short-lived alternative conformers since the

119   S-S bound species accumulates over time. These experiments were performed in a $dsbA^-$

120　background, such that S-S bonds formed after FhaC biogenesis and thus exclusively resulted from

121　its conformational changes in the membrane. We combined Cys residues in surface loops

122　(positions 224 in L1, 290 in L3, 342 in L4, 391 in L5, 503 in L7 and 545 in L8) with periplasmic

123　Cys residues in the POTRA2 domain (positions 167, 176, 195), in the POTRA1 domain (position

124　86) or in the linker (positions 33, 48) (Figure 2A). None of the single Cys substitutions markedly

125　affected the secretion activity of FhaC (Baud et al., 2014; Guerin et al., 2014; Guerin et al., 2015).

126　Under non-reducing conditions, partial oxidation of FhaC as detected by abnormal migration in

127　SDS-PAGE was identified for the combinations $Cys^{48}+Cys^{224}$, $Cys^{176}+Cys^{224}$, $Cys^{48}+Cys^{545}$ and

128　$Cys^{195}+Cys^{224}$, and weakly for $Cys^{167}+Cys^{224}$, indicating S-S bonds between the engineered Cys

129　residues (Figure 2B). Thus, the last portion of the linker, the α helix H4 and the b5-b6 β hairpin

130　of the POTRA2 domain can be found close to the extracellular loop L1, proximal to the B1-B16

131　β–barrel seam in specific conformers. To confirm S-S bond formation, the $FhaC^{C48+C224}$ and

132　$FhaC^{C195+C224}$ variants were overexpressed, purified and subjected to liquid chromatography

133　coupled to tandem mass spectrometry (MS) in reducing and non-reducing conditions. In both

134　variant samples, the regions that contain the Cys residues were detected only when proteolytic

135　digestion was performed after reduction and alkylation (Figure 2 Supplement 1), which supports

136　S-S bond formation between the linker and L1 in $FhaC^{C48+C224}$ and between the POTRA2 domain

137　and L1 in $FhaC^{C195+C224}$.

138

139　**Conformational changes of FhaC in a lipid environment**

140　 We made use of electron paramagnetic resonance (EPR) and nuclear magnetic resonance (NMR)

141　spectroscopies for their ability to characterize molecular structure and dynamics as well as minor

142　conformational states on complementary time scales and distance ranges (Mittermaier & Kay,

143   2009; Torricella et al., 2021). In addition, both techniques can be applied to proteins in lipid

144   bilayer environments i.e., liposomes and lipid nanodiscs (Liang & Tamm, 2016; Sahu & Lorigan,

145   2020).

146   We recorded NMR spectra of FhaC in liposomes and nanodiscs (Bayburt et al., 1998), using

147   solid- and solution-state NMR techniques, respectively. To render the 61-kDa protein more

148   accessible to NMR spectroscopy, we resorted to perdeuteration and specific ^{1}H, ^{13}C-isotope

149   labeling of isoleucine (Ile) δ_1 methyl groups (Ruschak & Kay, 2010). Since the 15 Ile residues of

150   FhaC are well distributed across all structural elements of the protein (Figure 3A), we expected

151   this reduced labeling scheme to nevertheless be able to report on larger-scale structural transitions

152   of FhaC. Signals from all Ile residues could be identified and assigned by Ile-to-Val mutations or

153   paramagnetic relaxation enhancement experiments (Amero et al., 2011; Venditti et al., 2011)

154   (Figure 3B,C). Broader signals in solid-state spectra are likely in part due to the choice of a sample

155   temperature of 17°C, below the phase transition for the majority of *E. coli* polar lipids, to achieve

156   longer-term sample stability and better signal-to-noise in dipolar coupling-based experiments.

157   However, we also suspect that FhaC exhibits conformational heterogeneity in proteoliposomes,

158   whereas it is more constrained in a nanodisc environment (see below).

159   Signal intensities of the Ile δ_1 methyls varied in both environments, informing on local

160   dynamics in the protein. Ile[14] was only visible in scalar coupling-based spectra, likely due to sub-

161   µs time scale motion towards the N-terminus of the protein, precluding its detection in spectra

162   based on dipolar couplings. The signal of Ile[548] in β-strand B16 at the barrel seam consistently

163   exhibited low intensity in both scalar and dipolar coupling-based spectra, indicating exchange

164   dynamics on the µs to ms time scale in this region. Moreover, the absence of through-space

165   correlations for all but the shortest distances expected from the crystal structure (Figure 3

7

166   Supplement 1) also supports the notion of dynamics in FhaC, at least at the level of Ile side chains.

167   However, ^{13}C rotating-frame ($R_{1\rho}$) relaxation dispersion experiments probing exchange between

168   states with different chemical shifts on the μs time scale (Lewandowski et al., 2011; Ma et al.,

169   2014) yielded statistically flat dispersion profiles (Figure 3 Supplement 2), indicating that the

170   conformational changes detected in FhaC by S-S cross-linking and EPR experiments likely occur

171   on slower time scales, or are not reflected in sizable Ile $C\delta_1$ chemical shift changes.

172   Continuous-wave EPR (CW-EPR) spectroscopy in X-band with site-directed spin labeling

173   typically detects transitions on time scales between 100 ps and 100 ns (Garcia-Rubio, 2020;

174   Organesyan et al., 2017), but also transitions beyond that time scale since distinct spin label

175   environments may generate spectral components reflecting conformational ensembles. Different

176   structural states of a protein that exchange with each other can thus be accessed by multi-

177   component spectral simulations. Among the few sites of FhaC accessible to nitroxide spin labelling

178   (Guerin et al., 2014; Guerin et al., 2015), we selected positions 33 in the linker, 187 and 195 in the

179   POTRA2 domain, and 503 in the extracellular loop L7 to engineer pairs of Cys residues and

180   labeled them with (1-oxyl-2,2,5,5-tetramethyl-Δ3-pyrroline-3-methyl) methanethiosulfonate

181   (MTSL). This yielded FhaC variants FhaC$^{33R1+503R1}$, FhaC$^{187R1+503R1}$, and FhaC$^{195R1+503R1}$, where

182   R1 represents the spin label. EPR spectra of the proteins in β-octyl glucoside (bOG) micelles

183   revealed hyperfine coupling values indicating contributions of several components, i.e., distinct

184   mobility regimes for one or both probes (Figure 4). The spectral features of FhaC$^{187R1+503R1}$ and

185   FhaC$^{195R1+503R1}$ both showed fast- and intermediate-motion components as expected for spin probes

186   exposed to solvent, whereas those of FhaC$^{33R1+503R1}$ indicated a slow-motion regime, most likely

187   at site 33 as observed earlier (Guerin et al., 2014).

188   The CW-EPR spectra of FhaC$^{195R1+503R1}$ and FhaC$^{187R1+503R1}$ in proteoliposomes exhibited

189   signal broadening and indicated several conformers (Figure 4; Figure 4 Supplement 1), providing

190   evidence for a dynamic protein that populates several conformational states. Spectral splitting

191   values around 7.0 mT reveal very slow motions of the probe, suggesting a change of its

192   environment most likely at positions 187 and 195 rather than 503, since no large spectral changes

193   between bOG and lipid environments were detected for FhaC$^{33R1+503R1}$. Such reduced mobility

194   might indicate interactions of the spin probes with the lipid bilayer. Spectra of FhaC were similar

195   in nanodiscs and in bOG, suggesting that for FhaC, the former do not fully reproduce the

196   membrane environment (Figure 4 Supplement 1). Thus, although residues 187 and 195 in the

197   POTRA2 domain are solvent-exposed in the crystal structure of FhaC, our EPR data highlight a

198   conformation where they may be close to the lipid bilayer.

199

200   **Shorter-than-expected distances between POTRA2 domain and extracellular side with**

201   **Pulsed Electron Double Resonance (PELDOR) spectroscopy**

202   Spin–spin distances between 1.8 and 8 nm in membrane proteins are accessible with PELDOR

203   spectroscopy and can provide insight into non-homogeneous conformational ensembles (Jeschke,

204   2012). For FhaC$^{195R1+503R1}$ and FhaC$^{187R1+503R1}$ in bOG, the main populated states correspond to

205   distance distributions between the two spin probes centered at 7.2 nm and 5.6 nm, consistent with

206   distances calculated using MTSL rotamer libraries attached to the corresponding residues of the

207   FhaC crystal structure (Figure 5A; Figure 5 Supplement 1). For FhaC$^{33R1+503R1}$ a broader distance

208   distribution was observed, with contributions centered at 4.2 nm and 4.6 nm as also predicted by

209   rotamer libraries (Figure 5 Supplement 1) (Jeschke, 2013, 2020).

210   In addition to the expected long distance, shorter distance distributions centered at 2.5 nm and

211   3.5 nm were observed for FhaC$^{195R1+503R1}$ in proteoliposomes that can be attributed to conformers

212   with the two probes closer to one another than in the crystal structure conformation (Figure 5B;

213   Figure 5 Supplement 2). PELDOR experiments also showed additional peaks in the distance

214   distributions for FhaC$^{33R1+503R1}$ and FhaC$^{187R1+503R1}$ in proteoliposomes, with shorter distances than

215   expected for the latter and both shorter and longer distances for the former (Figure 5B). Thus, for

216   the three variants, insertion in liposomes leads to the formation of multiple different conformations.

217   The point mutation Asp^{492}Arg disrupts a conserved salt bridge between L6 and the inner barrel

218   wall and induces conformational changes in FhaC (Guerin et al., 2015). We introduced the

219   Asp^{492}Arg substitution in FhaC$^{195R1+503R1}$ and performed EPR experiments. They showed an

220   increased proportion of species characterized by slow probe motions and short inter-spin distances

221   (Figure 5 Supplement 3). Hydrogen-deuterium exchange MS experiments confirmed the increased

222   conformational flexibility in several regions of FhaC^{R492} compared to its wild type (wt) counterpart

223   (Figure 5 Supplement 3).

224   Taken together, our results support the idea that the POTRA2 domain can undergo large

225   conformational changes, which are likely facilitated by the rupture of the L6-inner barrel wall

226   interaction. The H1-POTRA1 linker can also adopt several conformations and move towards the

227   cell surface.

228

229   **Evidence for proximity between the b5-b6 hairpin of the POTRA2 domain and the barrel**

230   **using paramagnetic relaxation enhancement (PRE) NMR**

231   To complement the EPR data, we performed PRE experiments in which a single MTSL probe is

232   attached to an engineered Cys in the protein, and attenuation of NMR signals of nuclei within a

233 radius of about 25 Å around the MTSL probe can be detected even if they only transiently approach

234 the probe (Battiste & Wagner, 2000). We chose residue 220 in the extracellular loop L1 for this

235 experiment. Intensities of Ile δ_1 methyl signals in FhaC^{220R1} measured by solid-state NMR in

236 proteoliposomes were referenced to those in a sample with a diamagnetic MTSL analog attached

237 to the same residue, FhaC^{220R1dia} (Nadaud et al., 2007). Comparison of the signal intensity ratios

238 obtained for different FhaC residues allows to determine whether a signal is more attenuated than

239 would be expected from the crystal structure, indicating a residue approaching the probe more

240 closely. Nevertheless, as the resultant para- versus diamagnetic signal intensity ratios do not

241 necessarily normalize to 1 chiefly due to variations in the amount of labeled protein between the

242 samples, we did not attempt to extract quantitative distance measurements from these data.

243   Ile^{114}, Ile^{136}, and Ile^{141} in the POTRA1 and POTRA2 domains are more than 38 Å apart from

244 the position of the paramagnetic MTSL on Cys^{220} according to an MTSL ensemble modeled onto

245 residue 220 in the crystal structure (Hagelueken et al., 2015) (Figure 6 Supplement Table 1). In

246 agreement with our other data that do not implicate these residues in any large-scale

247 conformational changes, we found the highest para- versus diamagnetic intensity ratios (i.e., no

248 attenuation) for their NMR signals (Figure 6A,B). Conversely, Ile^{27}, Ile^{441}, Ile^{506}, and Ile^{548} are

249 expected to be within 16 to 25 Å of the paramagnetic center; correspondingly, their signals were

250 attenuated. In agreement with expected distances to the paramagnetic center of 12 and 32 Å for

251 Ile^{252} and Ile^{420}, respectively, the overlapped signal due to these two residues exhibited

252 intermediate attenuation. Finally, the signal of Ile^{188} in strand b5 of the POTRA2 domain was

253 attenuated more than would be expected for a residue at 35 Å distance from the paramagnetic

254 center. The difference in attenuation with respect to the reference residues Ile^{114}, Ile^{136}, and Ile^{141}

255 is significant (p < 0.05). In line with our results from cross-linking and EPR spectroscopy, this

256   result thus supports the notion that regions of the POTRA2 domain encompassing strand b5 can

257   approach the extracellular loops. Conversely, signals from the POTRA2 H4 helix (Ile[172], Ile[176],

258   Ile[179]) were not significantly attenuated compared to reference signals.

259   Notably, we did not obtain indications for alternative conformers in FhaC reconstituted into

260   nanodiscs with EPR or NMR spectroscopy (Figure 6 Supplement 2). Analysis of PELDOR

261   experiments on FhaC[195R1+503R1] yielded only a long distance between the spin labels, as expected

262   from the crystal structure, and PRE experiments on FhaC[195R1] showed attenuation of NMR signals

263   only within the POTRA2 domain. Along with smaller linewidths of FhaC NMR signals in

264   nanodiscs compared to liposomes (Figure 3B,C), these findings further support the idea that the

265   nanodisc environment constrains the conformational space accessible to FhaC.

266

267   **Interactions of portions of the POTRA2 domain with the β barrel by native mass**

268   **spectrometry**

269   Our data imply that the POTRA2 domain undergoes some breaking up in the secretion cycle. We

270   thus investigated its lability by using structural MS-based approaches in bOG micelles (Figure 7).

271   Native MS analysis of FhaC revealed a monomer that could be stripped of bOG at 60 V, a relatively

272   low collision energy (CE), and that displayed a narrow charge state distribution between 14+ and

273   19+ indicative of a folded protein in a single conformation (Figure 7 Supplement 1).

274   We used collision-induced unfolding (CIU) (Tian et al., 2015) to characterize the stability and

275   the organization of the FhaC domains. FhaC displayed two transitions at 60 V and 120 V as shown

276   by the increases of collision cross section (CSS) values (Figure 7C). As the number of transitions

277   in the gas phase can generally be related to the number of domains of a protein (Zhong et al., 2014),

278   and extra-membrane domains are more likely to experience early unfolding than domains

279 embedded in detergent or lipids due to collisional cooling (Barrera et al., 2009), those transitions

280 might be caused by unfolding of the POTRA domains and/or ejection and unfolding of H1. Control

281 CIU experiments with other *B. pertussis* outer membrane proteins (OMPs) with small soluble

282 domains inside their β barrels, the TonB-dependent transporter BfrG and the translocator domain

283 of an autotransporter, SphB1-$\alpha\beta$, showed a single unfolding transition at low voltage, which likely

284 corresponds to unfolding of these soluble domains (Figure 7 Supplement 2). Thus, the β barrels of

285 these three proteins likely remain structurally intact at high activation conditions, most likely due

286 to strong hydrogen bonding networks.

287   To further investigate whether the CIU transitions observed for FhaC stem from unfolding of

288 the POTRA domains or ejection of the H1 helix, we studied the CIU pathway of FhaC$^{C4+C391}$ in

289 which H1 is locked inside the barrel by an S-S bond and thus cannot move out (Guerin et al., 2014).

290 FhaC$^{C4+C391}$ exhibited the same transitions as wt FhaC, although the second unfolding event was

291 delayed by 30 V and the overall CCS value was increased by 50 Å^2 (Figure 7 Supplement 3). As

292 CIU is unlikely to break S-S bonds (Tian et al., 2015), comparison of these unfolding pathways

293 suggests that the two transitions correspond to successive unfolding of the POTRA domains, with

294 the barrel remaining intact in those conditions. H1 stays inside the barrel or its unfolding barely

295 registers in the CCS values. The delay of the second unfolding transition for FhaC$^{C4+C391}$ suggests

296 that locking H1 in the barrel stabilizes one of the POTRA domains, although from the data we

297 cannot discern which one.

298   We next tested the possibility that portions of the POTRA2 domain might bind to the β barrel,

299 probably along strands B1 or B16 upon opening of the lateral seam. Using native MS, we assessed

300 the binding of synthetic peptides that correspond to various periplasmic portions of FhaC,

301 including b5-b6 (2815 Da), b4+L (*i.e.*, b4 followed by the b4-H3 linker; 2210.5 Da) and L+H4

13

302   (*i.e.*, the H3-H4 linker followed by H4; 2836 Da) of the POTRA2 domain, Fha-NT (2178.5 Da),

303   the N-terminal β hairpin of the FhaB transport substrate, b2-b3 of the POTRA1 domain (2496 Da),

304   and Lk (2597 Da), a non-structured peptide from the linker region between H1 and the POTRA1

305   domain (Figure 8; Figure 8 Supplement 1). The same experiments were performed with SphB1-

306   αβ to correct for non-specific binding, which might occur in native MS experiments due to artifacts

307   induced by interaction with the detergent during the electrospray process (Landreh et al., 2016).

308   Fha-NT, b4+L and b5-b6 exhibited binding to FhaC, with b5-b6 binding at the highest level and

309   in two copies, but markedly less to the FhaC$^{C4+C391}$ variant (Figure 8A-C; Figure 7 Supplement 3).

310   We assessed structural changes induced by peptide binding using native ion-mobility (IM)

311   MS. At low CE (*i.e.*, no activation), all three peptides increased the CCS of the compact state of

312   FhaC by rather small increments of 91-92 Å^2 (Figure 9; Figure 9 Supplement 1). However, upon

313   increasing the activation conditions, Fha-NT and b4+L no longer increased the CCS of FhaC,

314   compared to the unbound protein. In contrast, the b5-b6 peptide caused an increase in CCS values

315   both at low and high collisional activation, suggesting that a structural change was induced upon

316   peptide binding and that the peptide was bound to a region that remains folded in these conditions

317   (Figure 9). As our CIU studies suggest that the POTRA domains likely unfold at high CE, the

318   effect of b5-b6 on the CCS might thus stem from peptide binding to the β barrel. The same

319   experiment with FhaC$^{C4+C391}$ showed a lower level of peptide binding, which nevertheless caused

320   a similar increase of CCS at both low and high energies, like with wt FhaC (Figure 9C and Figure

321   7 Supplement 3). This supports the model that the b5-b6 hairpin the POTRA2 domain undergoes

322   a large reorientation to interact with the barrel, facilitated by the ejection of H1. Given the

323   amphipathic nature of this hairpin, it might align with an edge of the open β-barrel seam.

324

325 **DISCUSSION**

326 As Omp85 transporters are thought to perform their functions in the absence of an energy source

327 in the periplasm, their postulated conformational cycling must involve low energy barriers between

328 conformers, as reported for BamA (Xiao et al., 2021). Here, we obtained evidence for large

329 conformational changes of FhaC that involve portions of the POTRA2 domain approaching the

330 lipid bilayer and the extracellular side of the protein. Conformational changes of FhaC occur

331 independently of the presence of the substrate, indicating that such dynamics is an intrinsic

332 structural feature of the protein, most likely with implications for its function. Notably, the

333 conformational states appear to be in slow equilibrium, as with BamA (Hartmann et al., 2018).

334 All structural elements of TpsB transporters are connected with one another, structurally and

335 functionally, and therefore their motions are likely to be coupled (Guerin et al., 2014; Guerin et

336 al., 2020; Guerin et al., 2015; Maier et al., 2015). In the resting conformation, H1 and L6 interact

337 with the barrel wall, H1 with L1, the H1-POTRA1 linker with the POTRA domains, and the

338 POTRA2 domain with the periplasmic side of the barrel (Guerin et al., 2020; Maier et al., 2015).

339 In the secretion process, L6 breaks its connection with the barrel wall, H1 moves towards the

340 periplasm, and part of the B1-B16 seam unzips (Guerin et al., 2014; Guerin et al., 2020; Guerin et

341 al., 2015). Here we have shown that these motions are also coupled to substantial conformational

342 changes of the POTRA2 domain. In CdiB[Ab], coordinated motions of the first barrel strand B1 and

343 the extracellular loops L1, L2 and L6 favor the active conformation of the transporter (Guerin et

344 al., 2020). Based on this and previous work we thus propose that concerted conformational changes

345 lead to channel opening and substrate entry.

346 Lateral opening of the barrel is a common feature of Omp85 transporters. For BamA and Sam50,

347 the B1 strand at the lateral gap templates folding of client proteins by β augmentation (Doyle &

15

348   Bernstein, 2019; Höhr et al., 2018, Tomasek, 2020 #30). In TpsB transporters, lateral opening is

349   required for secretion (Guerin et al., 2020), and this work indicates that it is coupled to motions of

350   part of the POTRA2 domain towards the β barrel. EPR, NMR and S-S cross-linking data revealed

351   the proximity of parts of the POTRA2 domain to the lipid bilayer or to the extracellular side of

352   FhaC in some conformers, and structural MS experiments showed the binding of the POTRA2 b5-

353   b6 hairpin peptide to the β barrel under conditions in which the POTRA domains are very likely

354   unfolded. This binding might involve β augmentation of the B1 strand in an unzipped

355   conformation by the b5-b6 hairpin, as suggested by our IM-MS results and by the *in vivo* formation

356   of an S-S bond between the tip of that hairpin and the extracellular loop L1. The b5-b6 sequence

357   fits ideally in the open seam, with its amphipathic nature and suitable charge partitioning. By

358   utilizing intrinsic protein dynamics, TpsB transporters mediate protein secretion without the need

359   for cofactors or external energy sources. Although such conformational changes are unprecedented

360   in the Omp85 superfamily, divergent functional evolution has necessarily implied specific

361   mechanistic adaptations.

362   How the motions of the POTRA2 domain and the H1 helix are coordinated remains

363   speculative. According to MD simulations on CdiB[Ab], breaking the connections between the loops

364   L1 and L6 favors expulsion of H1 from the barrel, which elicits barrel unzipping between B1 and

365   B16 (Guerin et al., 2020). Disruption of the B1-B16 seam might trigger a swing motion of the b5-

366   b6 hairpin of the POTRA2 domain toward the open seam, enlarging the barrel by β augmentation.

367   Importantly, the groove between H4 and b5 in the POTRA2 domain is a binding site for the

368   conserved TPS domain of the FhaC substrate, FhaB (Delattre et al., 2011), and therefore such a

369   conformational change of the POTRA2 domain might hoist a portion of the bound substrate

370   towards the barrel. As the alternative conformations of FhaC exist in the absence of its substrate,

371 the conformational changes occur spontaneously, on a slow time scale (ms or above). The

372 incoming FhaB substrate would interact with conformations in which its binding site on FhaC is

373 accessible in the periplasm (Maier et ao., 2015) and piggyback on spontaneous motions of its

374 transporter to initiate secretion, thereby displacing the equilibrium between conformations. Recent

375 work has indicated that energy may be transduced from the inner membrane to the BAM complex

376 through the protonmotive force-utilizing SecDF complex (Alvira et al., 2020). One cannot rule out

377 that the intrinsic conformational changes of FhaC *in vivo* are similarly enhanced by an energy-

378 transducing mechanism. The observation that portions of the linker also approach the extracellular

379 loops as seen in the cross-linking experiments might reflect futile conformational changes

380 involving the linker in place of the substrate, in the absence of the latter. Notably, evidence for the

381 last part of the linker reaching the cell surface was obtained previously (Guedin et al., 2000).

382 As the POTRA2 domain partially breaks up during secretion, it must reassemble after

383 secretion is completed. This may be mediated by the interactions of the H3 helix and the barrel-

384 proximal end of b5 of the POTRA2 domain with the periplasmic turn T1 of the barrel, which are

385 important for FhaC activity. These fixed points of the POTRA2 domain may ensure that FhaC can

386 regain its resting conformation after secretion, which is necessary to limit OM permeability.

387 Consistent with this hypothesis, disrupting the conformation of the periplasmic turn T1 yielded

388 transient, very large channels as detected in electrophysiology experiments (Méli et al., 2006). Our

389 model for the mechanism of protein transport in TPS systems recapitulates currently available data

390 and establishes mechanistic links between TpsBs and other Omp85 transporters.

391

392 **Materials and Methods**

393 **Strains and plasmids**

394   *E. coli* JCB570 or JCB571 (*dsbA*::kan) were used for low level expression of FhaC and *E. coli*

395   BL21(DE3-*omp5*) for overexpression. For peptide mapping FhaC$^{C48+C224}$ and FhaC$^{C195+C224}$ were

396   overexpressed in BL21(DE3-*omp5 dsbA::kan*), which was constructed as described in (Derbise et

397   al., 2003). Point mutations in *fhaC* were generated using the QuikChange II XL Kit (Agilent, Les

398   Ulis, France) on pFc3 (Guedin et al., 2000). Overexpression of FhaC for purification was

399   performed from pET22 or pET24 plasmids (Clantin et al., 2007). ptacFha44-His codes for the first

400   80 kDa of the FhaC substrate FhaB, called Fha44, followed by a 6-His tag. It was constructed by

401   adding a 1.2-kb Sal-BamHI fragment of the *fhaB* gene into the same sites of the ptacNM2lk-His

402   plasmid (Guerin et al., 2015). pFJD63 codes for FhaC under the control of the P$_{BAD}$ promoter

403   (Guedin et al., 1998). Its derivatives were constructed by ligating the XhoI-HindIII and XhoI-XbaI

404   fragments of pFJD63 with the XbaI-HindIII *fhaC* fragments with the relevant mutations from the

405   pFc3 derivatives. pMSP1D1 and pMSP1E3D1 were obtained from Addgene (Watertown, MA,

406   USA). pSphB1αβ is a derivative of pT7SBαβ (Dé et al., 2008) with a 6-His tag. To construct

407   pT7bfrG-H, the sequence corresponding to the mature protein was PCR amplified and inserted in

408   pFJD138 (Méli et al., 2006) after the signal-peptide and 6-His tag sequences.

409

410   ***In vivo* assays**

411   To monitor S-S bond formation *in vivo*, the pFc3 variants were introduced in *E. coli* JCB571. The

412   recombinant bacteria were grown at 37°C in minimum M9 medium containing 0.1%

413   casaminoacids under agitation. The cells were collected by centrifugation when the optical

414   densities at 600 nm (OD$_{600}$) of the cultures reached 0.8. The cell pellets were resuspended in 50

415   mM sodium (pH 6.8) containing 10 mM N-ethylmaleimide and lysed using a Hybaid ribolyzer

416   apparatus (50 sec at speed 6). The membranes were collected by ultracentrifugation of the clarified

18

417 lysates at 90,000 g for 1 h. The pellets were resuspended in loading buffer without reducing agent

418 and separated into two aliquots, with DTE added at 25 mM to one of them before heating at 70°C

419 for 10 min. FhaC was detected using anti-FhaC antibodies (Delattre et al., 2011) with alkaline

420 phosphatase development for 15 min.

421 For the secretion assays, overnight cultures of *E. coli* JCB570 or JCB571 harboring a pFJD63

422 derivative and ptacFha44-His were diluted to OD_{600} of 0.3 in LB and grown under agitation with

423 0.01% arabinose for 20 min to produce FhaC. The bacteria were collected by centrifugation,

424 resuspended in prewarmed LB without arabinose and grown to OD_{600} of 0.8 before adding IPTG

425 at 1 mM to induce the expression of Fha44. Culture aliquots were collected 5 and 20 min thereafter

426 and placed on ice. After centrifugation to harvest the bacteria, Fha44 was affinity-purified from

427 the supernatants with Ni-NTA beads (Qiagen, Courtaboeuf, France). The membrane extracts were

428 prepared and FhaC was detected as above. Fha44 was detected by immunoblotting using anti-6His

429 antibodies, the ECL kit of Amersham (Merck, St Quentin-Fallavier, France) and the Amersham

430 Imager 600 (GE) with 1 sec exposure. The amounts of Fha44 in supernatants were quantified with

431 ImageJ.

432

433 **Protein Purification and spin labeling**

434 The production and purification of the FhaC derivatives was performed as described (Guerin et al.,

435 2014). Expression for NMR experiments was performed in M9 minimal medium in D_2O, 2.5 g/L

436 ^{2}H-glucose (Sigma, St Quentin-Fallaviers, France), 1g/L ^{15}N-NH4Cl, 1g/L ^{15}N,^{2}H-isogro (Sigma)

437 and ^{13}C-α-ketobutyric acid (Sigma) to achieve u-(^{2}H,^{15}N), Ile-δ_1(^{13}CH$_3$) isotope labeling (Ruschak

438 & Kay, 2010). For spin labeling, 3 mM tris(2-carboxyethyl)phosphine (TCEP, Sigma) was added

439 to the detergent extract before ion exchange chromatography. The FhaC-containing fractions were

440   mixed with a 10-fold molar excess MTSL or its diamagnetic analogue (1-Acetoxy-2,2,5,5-

441   tetramethyl-δ-3-pyrroline-3-methyl) methanethiosulfonate (Toronto Research Chemicals, North

442   York, ON, Canada) at 15°C with gentle agitation for 16 hours. Excess MTSL was removed by

443   chromatography. SphB1-αβ and BfrG were produced from *E. coli* BL21(DE3-*omp5)* and purified

444   from bOG extracts using Ni^{2+} affinity chromatography. For BfrG 300 mM NaCl was added to

445   improve solubility.

446

447   **Preparation of liposomes and nanodiscs and protein reconstitution**

448   Small unilamellar vesicles (SUVs) from *E. coli* polar lipids, dimyristoyl phosphatidyl choline

449   (DMPC) or mixtures of DMPC and dimyristoyl phosphatidyl glycerol (DMPG) (Avanti, Interchim,

450   Montluçon, France) at the indicated ratios were prepared as described (Guerin et al., 2014). The

451   SUVs were mixed with FhaC variants at lipid:protein molar ratios of approx. 2500:1 for EPR and

452   200:1 for NMR experiments, respectively, at room temperature, with gentle agitation for one hour.

453   The proteoliposomes were formed by removal of detergent with the progressive addition of

454   Biobeads SM2 (Bio-Rad), and the proteoliposomes were collected by ultracentrifugation. All steps

455   were performed under argon. Final buffer concentrations after mixing FhaC and liposomes were

456   about 12.5 mM each of Tris and NaP_i, 150 mM NaCl, pH 6.7.

457   Nanodiscs were prepared with the MSP1D1 and MSP1E3D1 scaffold proteins (Ritchie et al.,

458   2009) produced in *E. coli* BL21(DE3), with an induction of 3 h at 28°C. For NMR experiments,

459   scaffold proteins were expressed in M9 minimal medium in D_2O using ^2H-glucose as carbon

460   source to suppress their signals in the $(^1H,^{13}C)$-based NMR spectra. The bacteria were broken using

461   a French press in 50 mM Tris-HCl (pH 8), 300 mM NaCl (TN buffer), 1% Triton X100 (TNX

462   buffer), and the clarified lysates were subjected to Ni^{2+} affinity chromatography. After successive

463 washes in TNX, TN buffer with 50 mM cholate, 20 mM and 50 mM imidazole, the proteins were

464 eluted in TN buffer with 400 mM imidazole, concentrated by ultrafiltration and dialyzed against

465 20 mM Tris-HCl (pH 8), 200 mM NaCl and 0.1 mM EDTA. DMPC and DMPG at a 2:1 ratio were

466 solubilized in chloroform, lyophilized overnight and resuspended to 25 mM in 20 mM Tris-HCl

467 (pH 7.5), 100 mM NaCl, 0.5 mM EDTA, 50 mM cholate. For NMR experiments, deuterated (d_{54}-)

468 DMPC and DMPG (Cortecnet, Voisins-le-Bretonneux, France) were used. FhaC, the scaffold

469 protein and the lipids were mixed at a ratio of 1:3:180, cholate was added to 15 mM, and incubation

470 performed for 1 h at room temperature. Biobeads were added progressively, and the incubation

471 was continued at 4°C overnight. The nanodiscs were collected by ultracentrifugation and

472 concentrated by ultrafiltration. For NMR experiments, the buffer was exchanged to 100 mM NaP_i

473 in D_2O pH* 7.2 using a 2-ml ZebaSpin column (7 kDa MWCO).

474

NMR experiments

476 For solid-state NMR experiments on FhaC variants reconstituted into liposomes, the

477 proteoliposomes collected by ultracentrifugation were transferred to 1.3 mm magic-angle-spinning

478 (MAS) solid-state NMR rotors (Bruker Biospin, Wissembourg, France) using an

479 ultracentrifugation device (Bertini et al., 2012) (Giotto Biotech, Sesto Fiorentino, Italy) in a

480 Beckman ultracentrifuge (SW 32 Ti rotor, 77,000 x g, 12°C, 30 – 60 min). NMR experiments were

481 performed on spectrometers operating at 800 and 950 MHz [1]H Larmor frequency (18.8 and 22.3

482 T magnetic field) (Bruker Biospin) at a MAS frequency of 50 kHz. Sample temperature was kept

483 at about 17°C as judged by the chemical shift of the bulk water resonance. Spectra were indirectly

484 referenced to 2,2-dimethyl-2-silapentane-5-sulfonate (DSS) via the lipid methylene proton

485 resonance, which appears at 1.225 ppm under our experimental conditions. Typical pulse lengths

21

486 for ^{1}H and ^{13}C hard 90° pulses were 2.1 and 3.8 µs, respectively. For cross-polarization (CP), field

487 strengths were 21 and 30 kHz for ^{1}H and ^{13}C, respectively (n=1 double-quantum Hartmann-Hahn

488 condition), with a 50-to-100% ramp on the ^{1}H radiofrequency (RF) field and a duration of 1.5 ms.

489 ^{1}H-detected 2D ^{13}C-^{1}H dipolar hCH correlation spectra (Barbet-Massin et al., 2014) were typically

490 recorded with 1600 data points and a spectral width of 40 ppm in the direct ^{1}H dimension and 100

491 to 140 data points and a spectral width of 13 ppm in the indirect ^{13}C dimension. For water

492 suppression, the MISSISSIPPI scheme (Zhou & Rienstra, 2008) at 15 kHz ^{1}H RF field with a

493 duration of typically 200 ms was employed. For the 2D hChH correlation spectrum, a ^{1}H-^{1}H

494 mixing time of 6.4 ms using radio frequency driven recoupling (Bennett et al., 1992) with a ^{1}H

495 field strength of 120 kHz was applied between back-CP and acquisition. ^{13}C $R_{1\rho}$ spectra

496 (Lewandowski et al., 2011; Ma et al., 2014) were recorded in a pseudo-3D fashion, with the ^{13}C

497 spinlock period inserted between the initial CP and the ^{13}C indirect evolution of the hCH sequence.

498 Spinlock field strengths from 1.2 to 10 kHz were used, and 5 spinlock durations from 2.5 to 80 ms

499 with one repeated value were recorded for each spinlock. The spinlock carrier frequency was kept

500 at the center of the isoleucine δ_1 methyl ^{13}C region, as in all other hCH correlation spectra. A ^{1}H

501 180° pulse was inserted in the middle of the spinlock period to suppress chemical shift anisotropy

502 / dipolar coupling cross-correlated relaxation (Kurauskas et al., 2016). Solid-state PRE NMR

503 experiments were recorded on FhaC samples with either a paramagnetic MTSL tag or a

504 diamagnetic MTSL analogue (Nadaud et al., 2007) attached to a Cys, reconstituted into *E. coli*

505 polar lipid liposomes. Standard dipolar 2D hCH correlation spectra were recorded.

506 Solution-state NMR experiments on FhaC in nanodiscs were conducted on a 900 MHz

507 spectrometer (Bruker Biospin) at 32°C sample temperature. Standard ^{13}C-^{1}H heteronuclear

508 multiple-quantum coherence (HMQC) or SOFAST-HMQC (Schanda & Brutscher, 2005)

509 experiments were recorded with 2048 and 150 data points and spectral widths of 14 and 7.4 ppm

510 in direct ^{1}H and indirect ^{13}C dimensions, respectively. For PRE experiments, standard ^{13}C-^{1}H

511 HMQC spectra were recorded on a FhaC^{195R1} sample before and after reduction of the

512 paramagnetic MTSL tag with a 10-fold molar excess of ascorbic acid (Battiste & Wagner, 2000).

513 NMR spectra were processed with TopSpin 4.0.3 (Bruker Biospin) or NMRPipe (Delaglio et

514 al., 1995) and analyzed with Sparky (Lee et al., 2015) or CcpNMR (Vranken et al., 2005). For the

515 relaxation dispersion curves, effective transverse relaxation rates $R_{2,eff}$ (comprising intrinsic

516 transverse relaxation rate $R_{2,0}$ and any exchange contribution R_{ex}) were extracted from

517 experimental $R_{1\rho}$ values using separately recorded R_1 experiments (Palmer & Massi, 2006). For

518 PRE experiments, ratios of peak intensities in spectra of para- and diamagnetic species (FhaC^{220R1}

519 and FhaC^{220R1dia} for solid-state experiments, oxidized and reduced FhaC^{195R1} in case of the

520 solution-state experiments, respectively) were calculated. These para- versus diamagnetic signal

521 intensity ratios do not normalize to 1 in our case. In the solid-state experiments, this is most likely

522 due to variations between the samples in terms of efficiency of protein reconstitution into

523 liposomes and total amounts of sample transferred to the NMR rotor. Both in solid and solution

524 state, spectroscopic factors likely also play a role (incomplete longitudinal relaxation and thus

525 lower signal-to-noise in the spectra of diamagnetic samples due to the use of short inter-scan delays

526 of 1 s (Iwahara et al., 2007)). We have thus opted to normalize PRE ratios to the maximum ratio

527 observed in each experiment, which was always observed in one of the residues furthest from the

528 paramagnetic center (Ile^{136} in FhaC^{220R1}, Ile^{14} in FhaC^{195R1}). This is equivalent to normalizing

529 signals within each spectrum to a reference signal whose intensity is unaffected by PRE effects.

530 We then only analyzed relative signal attenuation levels, instead of attempting to extract

531   quantitative distance measures. Error bars of PRE intensity ratios were calculated based on spectral

532   noise levels (root-mean-standard deviation of the spectral noise) using standard error propagation.

533

534   **EPR Experiments**

535   Continuous-wave (CW) EPR spectra were recorded at room temperature on a Bruker EMX

536   spectrometer operating at X-band frequency (~9.8 GHz) and equipped with a Bruker ER 4123D

537   dielectric resonator. Spectra were recorded with 100-kHz field modulation with a sweep rate of

538   1.8 G/s and a modulation amplitude of 1 G. CW-EPR spectra were background-subtracted and

539   baseline-corrected. Spin concentrations were calculated by double integration of the field-

540   modulated spectrum and comparison to a standard curve of 4-hydroxy TEMPO free radical.

541   Labeling efficiencies were calculated as the spin concentration obtained by double integration

542   divided by the total protein concentration obtained from optical absorbance at 280 nm. Low

543   labeling efficiencies indicated that the Cys side chains at the four sites are not fully accessible to

544   solvent in the detergent micelle.

545   PELDOR experiments were performed at Q-band frequency (~34 GHz) using a Bruker

546   EleXsys E580 spectrometer equipped with an overcoupled Bruker EN 5107D2 resonator. Pulses

547   were generated with a Bruker SpinJet AWG and amplified with a 50 W TWT amplifier. The

548   experiments were performed at 50 K and 30 K using a variable-temperature cryogen-free system

549   (Oxford, Oxford, UK). The deadtime-free, four-pulse PELDOR sequence [$(\pi/2)$probe — $\tau 1$ —

550   (π)probe — $\tau 1 + t$ — (π)pump — $\tau 2 - t$ — (π)probe — $\tau 2$ — (echo)] was employed with a 200-ns

551     $\tau 1$ delay and $\tau 2$ delays ranging from 3,200 ns to 7,000 ns depending on the sample (Pannier et al.,

552   2000). Probe pulses were 10 ns $(\pi/2)$ and 20 ns (π) Gaussian-shaped pulses at a frequency

553   corresponding to the maximum of the resonator response function and a magnetic field value

554   corresponding to the high-field shoulder of the echo-detected field-swept spectrum. The pump

555   pulse was implemented as a 24-ns pulse centered at a frequency 55 MHz higher than the probe

556   frequency and corresponding to the maximum of the nitroxide field-swept spectrum. Raw time-

557   domain PELDOR traces were background-corrected using DeerAnalysis 2019 package (Jeschke

558   et al., 2006), and the resulting signals were power-scaled in MATLAB to suppress sum and

559   difference peaks arising from multispin effects. Distance distributions were then calculated from

560   the scaled and background-corrected PELDOR traces by Tikhonov regularization. For

561   FhaC$^{33R1+503R1}$, FhaC$^{187R1+503R1}$ and FhaC$^{195R1+503R1}$, distance distributions were predicted using a

562   pre-computed rotamer library of the MTSL spin probe attached to specific residues on the PDB

563   structure (Jeschke, 2020).

564

565   **Peptide mapping of FhaC variants**

566   Purified FhaC$^{C48+C224}$ and FhaC$^{C195+C224}$ variants were subjected to non-reducing SDS-PAGE, and

567   acrylamide bands corresponding to the oxidized forms of the two proteins were excised. They were

568   washed with 50 µL of acetonitrile/NH$_4$HCO$_3$ (75/25) four times and dehydrated with acetonitrile

569   (ACN), or incubated in 10 mM DTT in NH$_4$HCO$_3$ for 30 min at 57°C and 30 min room

570   temperature, followed by incubation in 55 mM iodoacetamide in 25 mM NH$_4$HCO$_3$ for 20 min in

571   the dark, 3 washes with NH$_4$HCO$_3$ and dehydration with ACN performed twice. The pH of the

572   samples was decreased to 2.0, digestion was performed with pepsin (0.01 µg/µL) (Promega,

573   Charbonnieres-les-Bains, France) at a 1:50 enzyme:substrate ratio at 37°C for 3 hours, and the

574   reaction was stopped by heating at 95°C for 10 min.

575   NanoLC-MS/MS analysis was performed using a nanoAcquity Ultra-Performance-LC (Waters,

576   Manchester, UK) coupled to a Q-Exactive Plus Orbitrap mass spectrometer (Thermo Scientific,

577   Illkirch, France). Peptides were trapped on a nanoACQUITY UPLC precolumn (C18, 180 μm x

578   20 mm, 5 μm particle size), and eluted from a nanoACQUITY UPLC column (C18, 75 μm x 250

579   mm, 1.7 μm particle size) at a constant temperature of 60°C. Mobile phases A and B were

580   composed of 0.1% formic acid in water and 0.1% formic acid in ACN, respectively. Peptides were

581   eluted with gradients of B from 1 to 8% for 2 min, 8 to 35% for 58 min, 35 to 90% for 1 min, 90%

582   for 5 min, 90 to 1% B for 1 min and a concentration of 1% B for 20 min, with a constant flow rate

583   of 400 nL/min. The source temperature of the mass spectrometer was set to 250°C and the spray

584   voltage at 1.8 kV. Full scan MS spectra were acquired in positive mode with a resolution of

585   140,000, a maximum injection time of 50 ms, and an AGC target value of $3x10^6$ charges. The 10

586   most intense multiply charged peptides per full scan were isolated using a 2 m/z window and

587   fragmented using higher energy collisional dissociation (normalized collision energy of 27).

588   MS/MS spectra were acquired with a resolution of 17,500, a maximum injection time of 100 ms

589   and an AGC target value of 1×10^5, and dynamic exclusion was set to 60 sec. The system was

590   fully controlled by XCalibur software v3.0.63, 2013 (Thermo Scientific) and NanoAcquity UPLC

591   console v1.51.3347 (Waters). The MS/MS data were interpreted using a local Mascot server with

592   MASCOT 2.5.0 algorithm (Matrix Science, London, UK). Spectra were searched with a mass

593   tolerance of 5 ppm for MS and 0.07 Da for MS/MS data, using none as enzyme. Oxidation (+15.99

594   Da), and carbamidomethylation (57.02 Da) were specified as variable modifications. Protein

595   identifications were validated with a Mascot ion score above 25.

596

597   **HDX-MS experiments**

598   Purified wt FhaC and the FhaC^{R492} variant were injected with an automated HDX system

599   encompassing a CTC PAL robot (Leap Technologies, Zwingen, Switzerland), and a nanoAcquity

26

600   UPLC system with HDX technology (Waters). The proteins were diluted and incubated at 20 °C

601   for different deuteration times (0.5, 2, 10, 30, and 60 min) in 10 mM K_2HPO_4, 10 mM KH_2PO_4,

602   400 mM NaCl, 3% bOG, (pD 6,6) deuterated buffer. The exchange reaction was stopped by adding

603   1:1 (v/v) of 2 M Guanidine-HCl, 100 mM Glycine (pH 2.2) quench buffer at 1 °C for 0.5 min.

604   Quenched samples were then digested (100-pmole injections) through a pepsin-immobilized

605   cartridge (Enzymate pepsin column, 300 Å, 5 μm, 2.1 × 30 mm, Waters) in 0.1% aqueous formic

606   acid solution, and the generated peptides were trapped on UPLC ACQUITY BEH C18 VanGuard

607   precolumn of 2.1mm I.D. × 5 mm and 1.7 μM particle diameter (Waters) at 200 μl.min^{-1}. The

608   peptides were then separated on an ACQUITY UPLC BEH C18 column of 1.0mm I.D. × 100 mm,

609   1.7 μM particle diameter (Waters) at 0.1 °C with a gradient elution of A (0.1% formic acid

610   aqueous) and B (ACN with 0.1% formic acid) [2–40% B (7 min), 40–85% B (0.5 min), and 85%

611   B (1 min)] at a flow rate of 40 μL.min^{-1}. Mass spectrometry analyses were conducted on a Synapt

612   G2 HDMS (Waters) with an electrospray ionization in positive polarity, initially calibrated and

613   using a lock-mass correction with glufibrinogen peptide. Analyses were carried out in data-

614   independent acquisition mode (MSE, Waters) with the following parameters: ESI voltage, 3.2 kV;

615   cone voltage, 40 V; source temperature, 80 °C; desolvation gas, nitrogen at 150 °C and 800 L.h^{-1};

616   acquisition range, m/z 50–2000; scan time, 0.3 s; trap MS collision, 15 → 40 eV. MSE data were

617   processed using ProteinLynx Global Server 2.5.3 (Waters) with a custom protein sequence library,

618   where peptide and fragment tolerances were set automatically by PLGS, with oxidized methionine

619   (+15.99 Da) as variable modification. Data were then processed with DynamX 3.0 (Waters). All

620   experiments were carried out in triplicate and only peptides identified in all replicates were kept

621   with a minimum fragment of 0.2 per amino acid, a minimum intensity of 103, a length between 5

622   and 30 residues and a file threshold of 3. Deuterium uptakes for all identified peptides were

27

623   manually checked and validated. Only one charge state was kept for each peptide, and deuterium

624   uptake was not corrected for back-exchange, represented as relative. HDX-MS results were

625   statistically validated using a mixed effects model (MEMHDX71), with a P value set to 0.01.

626

627   **Native MS and ion mobility**

628   Purified FhaC was buffer exchanged into 100 mM ammonium acetate buffer, pH 6.8,

629   supplemented with 50 mM bOG using a P6 desalting column (Biorad, Marnes-la-Coquette,

630   France). Samples were directly infused with nano-electrospray ionization with in-house-prepared

631   gold-coated borosilicate glass capillaries with a spray voltage of +1.4 kV. Spectra were recorded

632   on a quadrupole TOF instrument (Synapt G2 HDMS with 32K quadrupole, Waters) optimized for

633   transmission of native, high-m/z protein assemblies. Critical voltages and pressures throughout the

634   instrument were 50 V, 10 V, 150 V and 15 V for the sampling cone, extraction cone, trap and

635   transfer collision cell, respectively, with pressures of 9 mbar, 1.47×10^{-2} mbar and 1.21×10^{-2}

636   mbar for the source, trap and transfer regions unless indicated otherwise. CIU ion mobility

637   experiments were performed with 50 V sampling cone; 50-200 V trap collision energy; 42 V trap

638   DC bias; and 15 V transfer collision energy. Pressures throughout the instrument were 9 and 1.46

639    $\times 10^{-2}$ mbar for the source and trap/transfer collision cells. All spectra were processed with

640   Masslynx v4.1 (Waters). Collision cross section calibration was performed using GDH, ADH,

641   ConA and PK as proteins standard as described (Allen et al., 2016). It should be noted that due to

642   the generally lower charge states observed for membrane proteins, and the increased collision

643   energies required (compared to soluble proteins) for gentle release of proteins from detergent

644   micelles, the CCS values reported here are less accurate and intended for qualitative comparison

645   rather than quantitative matching to theoretical models.

646

Peptide binding assays

647

648 Synthesized peptides were dissolved in DMSO to a final concentration of 100 mM and added to

649 the protein sample at final concentrations of 10 µM FhaC and 100 µM peptide. To correct for non-

650 specific and detergent-specific binding, SphB1-αβ was run at identical concentrations and

651 conditions. For both proteins the fraction of peptide-bound protein was calculated based on peak

652 intensities, after which the binding to the decoy protein was subtracted to correct for non-specific

653 binding.

654

655 **Acknowledgements**

667

668 **References**

669   Allen, S. J., Eaton, R. M., & Bush, M. F. (2016). Analysis of native-like ions using structures for lossless ion
670   manipulations. *Anal Chem, 88*(18), 9118-9126. https://doi.org/10.1021/acs.analchem.6b02089

671

672   Alvira, S., Watkins, D. W., Troman, L., Allen, W. J., Lorriman, J. S., Degliesposti, G., Cohen, E. J., Beeby, M.,
673   Daum, B., Gold, V. A., Skehel, J. M., & Collinson, I. (2020). Inter-membrane association of the Sec
674   and BAM translocons for bacterial outer-membrane biogenesis. *Elife, 9*.
675   https://doi.org/10.7554/eLife.60669

676

677   Amero, C., Asuncion Dura, M., Noirclerc-Savoye, M., Perollier, A., Gallet, B., Plevin, M. J., Vernet, T.,
678   Franzetti, B., & Boisbouvier, J. (2011). A systematic mutagenesis-driven strategy for site-resolved
679   NMR studies of supramolecular assemblies. *J Biomol NMR, 50*(3), 229-236.
680   https://doi.org/10.1007/s10858-011-9513-5

681

682   Barbet-Massin, E., Pell, A. J., Retel, J. S., Andreas, L. B., Jaudzems, K., Franks, W. T., Nieuwkoop, A. J., Hiller,
683   M., Higman, V., Guerry, P., Bertarello, A., Knight, M. J., Felletti, M., Le Marchand, T., Kotelovica,
684   S., Akopjana, I., Tars, K., Stoppini, M., Bellotti, V., Bolognesi, M., Ricagno, S., Chou, J. J., Griffin, R.
685   G., Oschkinat, H., Lesage, A., Emsley, L., Herrmann, T., & Pintacuda, G. (2014). Rapid proton-
686   detected NMR assignment for proteins with fast magic angle spinning. *J Am Chem Soc, 136*(35),
687   12489-12497. https://doi.org/10.1021/ja507382j

688

689   Barrera, N. P., Isaacson, S. C., Zhou, M., Bavro, V. N., Welch, A., Schaedler, T. A., Seeger, M. A., Miguel, R.
690   N., Korkhov, V. M., van Veen, H. W., Venter, H., Walmsley, A. R., Tate, C. G., & Robinson, C. V.
691   (2009). Mass spectrometry of membrane transporters reveals subunit stoichiometry and
692   interactions. *Nat Methods, 6*(8), 585-587. https://doi.org/10.1038/nmeth.1347

693

694   Battiste, J. L., & Wagner, G. (2000). Utilization of site-directed spin labeling and high-resolution
695   heteronuclear nuclear magnetic resonance for global fold determination of large proteins with
696   limited nuclear overhauser effect data. *Biochemistry, 39*(18), 5355-5365.
697   https://doi.org/10.1021/bi000060h

698

699   Baud, C., Guerin, J., Petit, E., Lesne, E., Dupre, E., Locht, C., & Jacob-Dubuisson, F. (2014). Translocation
700   path of a substrate protein through its Omp85 transporter. *Nat Commun, 5*, 5271.
701   https://doi.org/10.1038/ncomms6271

702

703   Bayburt, T. H., Carlson, J. W., & Sligar, S. G. (1998). Reconstitution and imaging of a membrane protein in
704   a nanometer-size phospholipid bilayer. *J Struct Biol, 123*(1), 37-44.
705   https://doi.org/10.1006/jsbi.1998.4007

706

707   Bennett, A. E., Griffin, R. G., Ok, J. H., & Vega, S. (1992). Chemical shift correlation spectroscopy in rotating
708   solids: Radio frequency-driven dipolar recoupling and longitudinal exchange. *J. Chem. Phys., 96*,
709   8624–8627.

710

711   Bertini, I., Engelke, F., Gonnelli, L., Knott, B., Luchinat, C., Osen, D., & Ravera, E. (2012). On the use of
712   ultracentrifugal devices for sedimented solute NMR. *J Biomol NMR, 54*(2), 123-127.
713   https://doi.org/10.1007/s10858-012-9657-y

714

715   Clantin, B., Delattre, A. S., Rucktooa, P., Saint, N., Meli, A. C., Locht, C., Jacob-Dubuisson, F., & Villeret, V.
716   (2007). Structure of the membrane protein FhaC: a member of the Omp85-TpsB transporter
717   superfamily. *Science, 317*(5840), 957-961. https://doi.org/10.1126/science.1143860

718

719   Dé, E., Saint, N., Glinel, K., Méli, A. C., Levy, D., & Jacob-Dubuisson, F. (2008). Influence of the passenger
720   domain of a model autotransporter on the properties of its translocator domain. *Mol Membr Biol,*
721   *25*(3), 192-202. https://doi.org/10.1080/09687680701771925

722

723   Delaglio, F., Grzesiek, S., Vuister, G. W., Zhu, G., Pfeifer, J., & Bax, A. (1995). NMRPipe: a multidimensional
724   spectral processing system based on UNIX pipes. *J Biomol NMR, 6*(3), 277-293.
725   https://doi.org/10.1007/BF00197809

726

727   Delattre, A. S., Saint, N., Clantin, B., Willery, E., Lippens, G., Locht, C., Villeret, V., & Jacob-Dubuisson, F.
728   (2011). Substrate recognition by the POTRA domains of TpsB transporter FhaC. *Mol Microbiol,*
729   *81*(1), 99-112. https://doi.org/10.1111/j.1365-2958.2011.07680.x

730

731   Derbise, A., Lesic, B., Dacheux, D., Ghigo, J.-M., & Carniel, E. (2003). A rapid and simple method for
732   inactivating chromosomal genes in *Yersinia*. *FEMS Immunol Med Microbiol, 38*, 113-116.
733   https://doi.org/10.1016/S0928-8244(03)00181-0

734

735   Diederichs, K. A., Ni, X., Rollauer, S. E., Botos, I., Tan, X., King, M. S., Kunji, E. R. S., Jiang, J., & Buchanan, S.
736   K. (2020). Structural insight into mitochondrial beta-barrel outer membrane protein biogenesis.
737   *Nat Commun, 11*(1), 3290. https://doi.org/10.1038/s41467-020-17144-1

738

739   Doerner, P. A., & Sousa, M. C. (2017). Extreme Dynamics in the BamA beta-Barrel Seam. *Biochemistry,*
740   *56*(24), 3142-3149. https://doi.org/10.1021/acs.biochem.7b00281

741

742   Doyle, M. T., & Bernstein, H. D. (2019). Bacterial outer membrane proteins assemble via asymmetric
743   interactions with the BamA beta-barrel. *Nat Commun, 10*(1), 3358.
744   https://doi.org/10.1038/s41467-019-11230-9

745

746   Estrada Mallarino, L., Fan, E., Odermatt, M., Muller, M., Lin, M., Liang, J., Heinzelmann, M., Fritsche, F.,
747   Apell, H. J., & Welte, W. (2015). TtOmp85, a beta-barrel assembly protein, functions by barrel
748   augmentation. *Biochemistry, 54*(3), 844-852. https://doi.org/10.1021/bi5011305

749

750   Fan, E., Fiedler, S., Jacob-Dubuisson, F., & Muller, M. (2012). Two-partner secretion of gram-negative
751   bacteria: a single beta-barrel protein enables transport across the outer membrane. *J Biol Chem,*
752   *287*(4), 2591-2599. https://doi.org/10.1074/jbc.M111.293068

753

754 Garcia-Rubio, I. (2020). EPR of site-directed spin-labeled proteins: A powerful tool to study structural
755   flexibility. *Arch Biochem Biophys, 684*, 108323. https://doi.org/10.1016/j.abb.2020.108323

756

757 Gu, Y., Li, H., Dong, H., Zeng, Y., Zhang, Z., Paterson, N. G., Stansfeld, P. J., Wang, Z., Zhang, Y., Wang, W.,
758   & Dong, C. (2016). Structural basis of outer membrane protein insertion by the BAM complex.
759   *Nature, 531*(7592), 64-69. https://doi.org/10.1038/nature17199

760

761 Guedin, S., Willery, E., Locht, C., & Jacob-Dubuisson, F. (1998). Evidence that a globular conformation is
762   not compatible with FhaC-mediated secretion of the Bordetella pertussis filamentous
763   haemagglutinin. *Mol Microbiol, 29*(3), 763-774. https://doi.org/10.1046/j.1365-
764   2958.1998.00970.x

765

766 Guedin, S., Willery, E., Tommassen, J., Fort, E., Drobecq, H., Locht, C., & Jacob-Dubuisson, F. (2000). Novel
767   topological features of FhaC, the outer membrane transporter involved in the secretion of the
768   *Bordetella pertussis* filamentous hemagglutinin. *J Biol Chem, 275*(39), 30202-30210.
769   https://doi.org/10.1074/jbc.M005515200

770

771 Guerin, J., Baud, C., Touati, N., Saint, N., Willery, E., Locht, C., Vezin, H., & Jacob-Dubuisson, F. (2014).
772   Conformational dynamics of protein transporter FhaC: large-scale motions of plug helix. *Mol
773   Microbiol, 92*(6), 1164-1176. https://doi.org/10.1111/mmi.12585

774

775 Guerin, J., Bigot, S., Schneider, R., Buchanan, S. K., & Jacob-Dubuisson, F. (2017). Two-partner secretion:
776   Combining efficiency and simplicity in the secretion of large proteins for bacteria-host and
777   bacteria-bacteria interactions. *Front Cell Infect Microbiol, 7*, 148.
778   https://doi.org/10.3389/fcimb.2017.00148

779

780 Guerin, J., Botos, I., Zhang, Z., Lundquist, K., Gumbart, J. C., & Buchanan, S. K. (2020). Structural insight
781   into toxin secretion by contact-dependent growth inhibition transporters. *Elife, 9*.
782   https://doi.org/10.7554/eLife.58100

783

784 Guerin, J., Saint, N., Baud, C., Meli, A. C., Etienne, E., Locht, C., Vezin, H., & Jacob-Dubuisson, F. (2015).
785   Dynamic interplay of membrane-proximal POTRA domain and conserved loop L6 in Omp85
786   transporter FhaC. *Mol Microbiol, 98*(3), 490-501. https://doi.org/10.1111/mmi.13137

787

788 Hagelueken, G., Abdullin, D., & Schiemann, O. (2015). mtsslSuite: Probing biomolecular conformation by
789   spin-labeling studies. *Methods Enzymol, 563*, 595-622.
790   https://doi.org/10.1016/bs.mie.2015.06.006

791

792 Hartmann, J. B., Zahn, M., Burmann, I. M., Bibow, S., & Hiller, S. (2018). Sequence-specific solution NMR
793   assignments of the beta-barrel insertase BamA to monitor its conformational ensemble at the
794   atomic level. *J Am Chem Soc, 140*(36), 11252-11260. https://doi.org/10.1021/jacs.8b03220

795
796 Heinz, E., & Lithgow, T. (2014). A comprehensive analysis of the Omp85/TpsB protein superfamily
797   structural diversity, taxonomic occurrence, and evolution. *Front Microbiol, 5*, 370.
798   https://doi.org/10.3389/fmicb.2014.00370

799
800 Höhr, A. I. C., Lindau, C., Wirth, C., Qiu, J., Stroud, D. A., Kutik, S., Guiard, B., Hunte, C., Becker, T., Pfanner,
801   N., & Wiedemann, N. (2018). Membrane protein insertion through a mitochondrial beta-barrel
802   gate. *Science, 359*(6373). https://doi.org/10.1126/science.aah6834

803
804 Iadanza, M. G., Higgins, A. J., Schiffrin, B., Calabrese, A. N., Brockwell, D. J., Ashcroft, A. E., Radford, S. E.,
805   & Ranson, N. A. (2016). Lateral opening in the intact beta-barrel assembly machinery captured by
806   cryo-EM. *Nat Commun, 7*, 12865. https://doi.org/10.1038/ncomms12865

807
808 Iadanza, M. G., Schiffrin, B., White, P., Watson, M. A., Horne, J. E., Higgins, A. J., Calabrese, A. N., Brockwell,
809   D. J., Tuma, R., Kalli, A. C., Radford, S. E., & Ranson, N. A. (2020). Distortion of the bilayer and
810   dynamics of the BAM complex in lipid nanodiscs. *Commun Biol, 3*(1), 766.
811   https://doi.org/10.1038/s42003-020-01419-w

812
813 Iwahara, J., Tang, C., & Marius Clore, G. (2007). Practical aspects of (1)H transverse paramagnetic
814   relaxation enhancement measurements on macromolecules. *J Magn Reson, 184*(2), 185-195.
815   https://doi.org/10.1016/j.jmr.2006.10.003

816
817 Jeschke, G. (2012). DEER distance measurements on proteins. *Annu Rev Phys Chem, 63*, 419-446.
818   https://doi.org/10.1146/annurev-physchem-032511-143716

819
820 Jeschke, G. (2013). Conformational dynamics and distribution of nitroxide spin labels. *Prog Nucl Magn*
821   *Reson Spectrosc, 72*, 42-60. https://doi.org/10.1016/j.pnmrs.2013.03.001

822
823 Jeschke, G. (2020). MMM: Integrative ensemble modeling and ensemble analysis. *Protein Sci*.
824   https://doi.org/10.1002/pro.3965

825
826 Jeschke, G., Chechik, V., Ionita, P., Godt, A., Zimmermann, H., Banham, J., Timmel, C. R., Hilger, D., & Jung,
827   H. (2006). DeerAnalysis – a comprehensive software package for analyzing pulsed ELDOR data
828   2006, 30, 473-498. *Appl Magnetic Reson, 30*, 473-498.

829
830 Knowles, T. J., Scott-Tucker, A., Overduin, M., & Henderson, I. R. (2009). Membrane protein architects:
831   the role of the BAM complex in outer membrane protein assembly. *Nat Rev Microbiol, 7*(3), 206-
832   214. https://doi.org/10.1038/nrmicro2069

833
834 Kurauskas, V., Weber, E., Hessel, A., Ayala, I., Marion, D., & Schanda, P. (2016). Cross-correlated relaxation
835   of dipolar coupling and chemical-shift anisotropy in magic-angle spinning R1rho NMR

836   measurements: Application to protein backbone dynamics measurements. *J Phys Chem B, 120*(34),
837   8905-8913. https://doi.org/10.1021/acs.jpcb.6b06129

838
839   Landreh, M., Marty, M., Gault, J., & Robinson, C. (2016). A sliding selectivity scale for lipid binding to
840   membrane proteins. *Curr Op Struct Biol, 39*, 54-60. https://doi.org/10.1016/j.sbi.2016.04.005

841
842   Lee, W., Tonelli, M., & Markley, J. L. (2015). NMRFAM-SPARKY: enhanced software for biomolecular NMR
843   spectroscopy. *Bioinformatics, 31*(8), 1325-1327. https://doi.org/10.1093/bioinformatics/btu830

844
845   Lewandowski, J. R., Sass, H. J., Grzesiek, S., Blackledge, M., & Emsley, L. (2011). Site-specific measurement
846   of slow motions in proteins. *J Am Chem Soc, 133*(42), 16762-16765.
847   https://doi.org/10.1021/ja206815h

848
849   Liang, B., & Tamm, L. K. (2016). NMR as a tool to investigate the structure, dynamics and function of
850   membrane proteins. *Nat Struct Mol Biol, 23*(6), 468-474. https://doi.org/10.1038/nsmb.3226

851
852   Ma, P., Haller, J. D., Zajakala, J., Macek, P., Sivertsen, A. C., Willbold, D., Boisbouvier, J., & Schanda, P.
853   (2014). Probing transient conformational states of proteins by solid-state R(1rho) relaxation-
854   dispersion NMR spectroscopy. *Angew Chem Int Ed Engl, 53*(17), 4312-4317.
855   https://doi.org/10.1002/anie.201311275

856
857   Maier, T., Clantin, B., Gruss, F., Dewitte, F., Delattre, A. S., Jacob-Dubuisson, F., Hiller, S., & Villeret, V.
858   (2015). Conserved Omp85 lid-lock structure and substrate recognition in FhaC. *Nat Commun, 6*,
859   7452. https://doi.org/10.1038/ncomms8452

860
861   Méli, A. C., Hodak, H., Clantin, B., Locht, C., Molle, G., Jacob-Dubuisson, F., & Saint, N. (2006). Channel
862   properties of TpsB transporter FhaC point to two functional domains with a C-terminal protein-
863   conducting pore. *J Biol Chem, 281*, 158-166. https://doi.org/10.1074/jbc.M508524200

864
865   Mittermaier, A. K., & Kay, L. E. (2009). Observing biological dynamics at atomic resolution using NMR.
866   *Trends Biochem Sci, 34*(12), 601-611. https://doi.org/10.1016/j.tibs.2009.07.004

867
868   Nadaud, P. S., Helmus, J. J., Hofer, N., & Jaroniec, C. P. (2007). Long-range structural restraints in spin-
869   labeled proteins probed by solid-state nuclear magnetic resonance spectroscopy. *J Am Chem Soc,
870   129*(24), 7502-7503. https://doi.org/10.1021/ja072349t

871
872   Noinaj, N., Gumbart, J. C., & Buchanan, S. K. (2017). The beta-barrel assembly machinery in motion. *Nat
873   Rev Microbiol, 15*(4), 197-204. https://doi.org/10.1038/nrmicro.2016.191

874

875 Noinaj, N., Kuszak, A. J., Balusek, C., Gumbart, J. C., & Buchanan, S. K. (2014). Lateral opening and exit pore
876   formation are required for BamA function. *Structure, 22*(7), 1055-1062.
877   https://doi.org/10.1016/j.str.2014.05.008

878

879 Noinaj, N., Kuszak, A. J., Gumbart, J. C., Lukacik, P., Chang, H., Easley, N. C., Lithgow, T., & Buchanan, S. K.
880   (2013). Structural insight into the biogenesis of beta-barrel membrane proteins. *Nature,*
881   *501*(7467), 385-390. https://doi.org/10.1038/nature12521

882

883 Organesyan, V. S., Chami, F., White, G. F., & Thomson, A. J. (2017). A combined EPR and MD simulation
884   study of a nitroxyl spin label with restricted internal mobility sensitive to protein dynamics. *J*
885   *Magnetic Resonance, 274*, 24-35.

886

887 Palmer, A. G., 3rd, & Massi, F. (2006). Characterization of the dynamics of biomacromolecules using
888   rotating-frame spin relaxation NMR spectroscopy. *Chem Rev, 106*(5), 1700-1719.
889   https://doi.org/10.1021/cr0404287

890

891 Pannier, M., Veit, S., Godt, A., Jeschke, G., & Spiess, H. W. (2000). Dead-time free measurement of dipole-
892   dipole interactions between electron spins. *J Magnetic Reson 142*, 331-340.

893

894 Renault, M., Bos, M. P., Tommassen, J., & Baldus, M. (2011). Solid-state NMR on a large multidomain
895   integral membrane protein: the outer membrane protein assembly factor BamA. *J Am Chem Soc,*
896   *133*(12), 4175-4177. https://doi.org/10.1021/ja109469c

897

898 Ritchie, T. K., Grinkova, Y. V., Bayburt, T. H., Denisov, I. G., Zolnerciks, J. K., Atkins, W. M., & Sligar, S. G.
899   (2009). Reconstitution of membrane proteins in phospholipid bilayer nanodiscs. *Methods Enzymol,*
900   *464*, 211-231. https://doi.org/10.1016/S0076-6879(09)64011-8

901

902 Ruschak, A. M., & Kay, L. E. (2010). Methyl groups as probes of supra-molecular structure, dynamics and
903   function. *J Biomol NMR, 46*(1), 75-87. https://doi.org/10.1007/s10858-009-9376-1

904

905 Sahu, I. D., & Lorigan, G. A. (2020). Electron paramagnetic resonance as a tool for studying membrane
906   proteins. *Biomolecules, 10*(5). https://doi.org/10.3390/biom10050763

907

908 Schanda, P., & Brutscher, B. (2005). Very fast two-dimensional NMR spectroscopy for real-time
909   investigation of dynamic events in proteins on the time scale of seconds. *J Am Chem Soc, 127*(22),
910   8014-8015. https://doi.org/10.1021/ja051306e

911

912 Tian, Y., Han, L., Buckner, A. C., & Ruotolo, B. T. (2015). Collision induced unfolding of intact antibodies:
913   Rapid characterization of disulfide bonding patterns, glycosylation, and structures. *Anal Chem,*
914   *87*(22), 11509-11515. https://doi.org/10.1021/acs.analchem.5b03291

915

916   Tomasek, D., Rawson, S., Lee, J., Wzorek, J. S., Harrison, S. C., Li, Z., & Kahne, D. (2020). Structure of a
917   nascent membrane protein as it folds on the BAM complex. *Nature, 583*(7816), 473-478.
918   https://doi.org/10.1038/s41586-020-2370-1

919

920   Torricella, F., Pierro, A., Mileo, E., Belle, V., & Bonucci, A. (2021). Nitroxide spin labels and EPR
921   spectroscopy: A powerful association for protein dynamics studies. *Biochim Biophys Acta Proteins
922   Proteom, 1869*(7), 140653. https://doi.org/10.1016/j.bbapap.2021.140653

923

924   Venditti, V., Fawzi, N. L., & Clore, G. M. (2011). Automated sequence- and stereo-specific assignment of
925   methyl-labeled proteins by paramagnetic relaxation and methyl-methyl nuclear Overhauser
926   enhancement spectroscopy. *J Biomol NMR, 51*(3), 319-328. https://doi.org/10.1007/s10858-011-
927   9559-4

928

929   Vranken, W. F., Boucher, W., Stevens, T. J., Fogh, R. H., Pajon, A., Llinas, M., Ulrich, E. L., Markley, J. L.,
930   Ionides, J., & Laue, E. D. (2005). The CCPN data model for NMR spectroscopy: development of a
931   software pipeline. *Proteins, 59*(4), 687-696. https://doi.org/10.1002/prot.20449

932

933   Warner, L. R., Gatzeva-Topalova, P. Z., Doerner, P. A., Pardi, A., & Sousa, M. C. (2017). Flexibility in the
934   periplasmic domain of BamA is important for function. *Structure, 25*(1), 94-106.
935   https://doi.org/10.1016/j.str.2016.11.013

936

937   Xiao, L., Han, L., Li, B., Zhang, M., Zhou, H., Luo, Q., Zhang, X., & Huang, Y. (2021). Structures of the beta-
938   barrel assembly machine recognizing outer membrane protein substrates. *FASEB J, 35*(1), e21207.
939   https://doi.org/10.1096/fj.202001443RR

940

941   Zhong, Y., Han, L., & Ruotolo, B. (2014). Collisional and coulombic unfolding of gas-phase proteins: High
942   correlation to their domain structures in solution *Angew. Chem, 53*(35), 9209-9212.
943   https://doi.org/10.1002/anie.201403784

944

945   Zhou, D. H., & Rienstra, C. M. (2008). High-performance solvent suppression for proton detected solid-
946   state NMR. *J Magn Reson, 192*(1), 167-172. https://doi.org/10.1016/j.jmr.2008.01.012
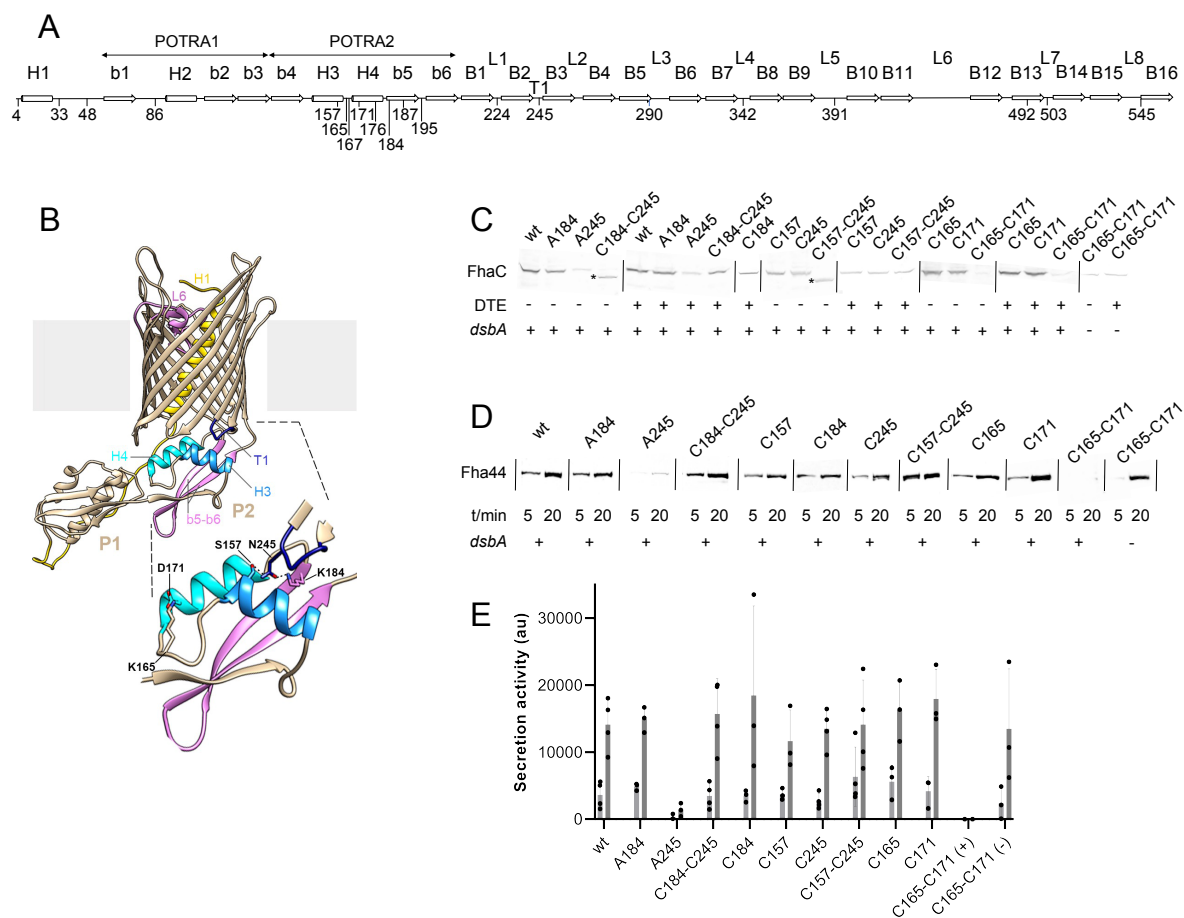
947

948

Figure 1. Effects of engineered S-S bonds on FhaC activity. (A) Linear representation of the secondary structure elements of FhaC, with residues used in this work. L1 to L8 represent the extracellular loops, b1 to b6 the β strands of the POTRA domains, H1 to H4 the α helices, and B1 to B16 the β−barrel strands. T1 is the first periplasmic turn. (B) Structural model of FhaC (PDB 4QKY). A zoom of the POTRA2 domain is shown below. (C) Residues involved in a salt bridge (Lys^{165}-Asp^{171}) or H bonds (Lys^{184}-Asn^{245}; Ser^{157}-Asn^{245}) in the resting conformation of FhaC were replaced as indicated (C=Cys; A=Ala). Immunoblots were performed on membrane extracts with anti-FhaC antibodies. The asterisks indicate oxidized species of FhaC detected in the absence of the reducing agent dithioerythritol (DTE) in the sample buffer. (D) The secretion activity of the FhaC variants was determined using a model substrate, Fha44-His, affinity precipitated from supernatants 5 and 20 min after induction. Immunoblots were developed with an anti-6His tag monoclonal antibody. (E) Quantification of Fha44 found in culture supernatants after 5 and 20 min. The means and standard deviations of the means are shown (n=3 or 4). Activity of $FhaC^{C165+C171}$ could only be detected in the *dsbA* KO strain (denoted C165-C171(-)), not in its wild type parent (denoted C165-C171(+)).
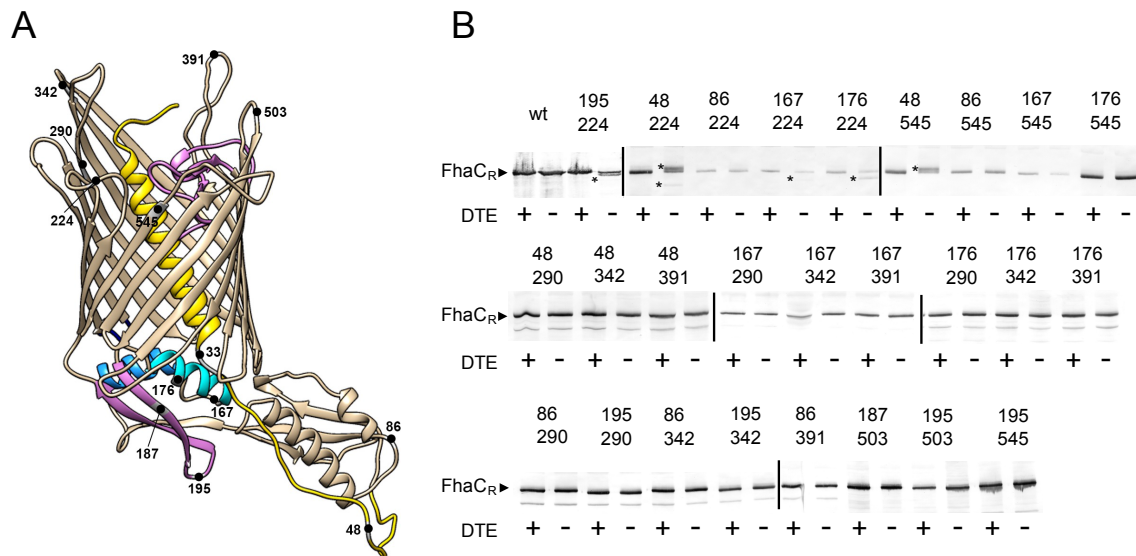
Figure 2. **Detection of transient conformers of FhaC *in vivo*.** (A) Position of the Cys substitutions in FhaC. (B) Immunoblot of membrane fractions of *E. coli JCB571* (*dsbA* KO strain) producing FhaC variants. The numbers indicate the positions of the two Cys residues. The reducing agent DTE was added to one half of each sample. FhaC_R represents the position of the reduced form. The asterisks point to the additional, cross-linked forms that can migrate faster or more slowly than the reduced form, depending on the respective positions of the two Cys residues. S-S bond formation was confirmed by mass fingerprinting analyses (Figure Supplement 1).

A C^{48}-C^{224}

```
  1 QAQGSLLPGA RDLNRIDDRQ RKEQLQRDIE RALTRPPVEL NPQSEAAAC
 51 RKPDATSGHT VTVHAVDLDF GVEGRLFDPA PLVQDYLNRP LDNEQLFLLV
101 KALSAALYDR GYATSIVTFV PPGVVDGVLK LKVEWGRIKG WLIDGKPLEG
151 TRDRMMVFSA MPGWQDKVLN VFDIDQAIYN INNGGKTGNI TIVPADEYGY
201 SYLDLQLQRR ALPRVSLGMD NSGPC PENG RYKYNASVTA NDLLGLNDTL
251 GLYIGNRYYR DAGHDAERNY DLMYSVPLGR TRLDLQTGYS TYRNLLKTRY
301 GQYQSAGNSR SFGLKATRLL YRDTRSQFSV YGGLKLRQNK NYLAGTRLDV
351 SSKHYSDVTV GMQYSTQRGA NAYFGDLSFT RGVGVNNGKY AAYDERGPQG
401 NVSRFNGSLA WTRYMALAGQ PIQWASQLGF QYSRQQLLNS YQITVGDEYT
451 VRGYNLRTSQ SGDSGVYLSN TLTVPVQFSL LGKQASVAPF VGADVGALKS
501 NHPDARTIRM AGLAAGVRFD LPYARMSFTY SKPVGAQPGG APRAPVWLYI
551 NAGLSF
```

B

```
  1 QAQGSLLPGA RDLNRIDDRQ RKEQLQRDIE RALTRPPVEL NPQSEAAAC
 51 RKPDATSGHT VTVHAVDLDF GVEGRLFDPA PLVQDYLNRP LDNEQLFLLV
101 KALSAALYDR GYATSIVTFV PPGVVDGVLK LKVEWGRIKG WLIDGKPLEG
151 TRDRMMVFSA MPGWQDKVLN VFDIDQAIYN INNGGKTGNI TIVPADEYGY
201 SYLDLQLQRR ALPRVSLGMD NSGPC PENG RYKYNASVTA NDLLGLNDTL
251 GLYIGNRYYR DAGHDAERNY DLMYSVPLGR TRLDLQTGYS TYRNLLKTRY
301 GQYQSAGNSR SFGLKATRLL YRDTRSQFSV YGGLKLRQNK NYLAGTRLDV
351 SSKHYSDVTV GMQYSTQRGA NAYFGDLSFT RGVGVNNGKY AAYDERGPQG
401 NVSRFNGSLA WTRYMALAGQ PIQWASQLGF QYSRQQLLNS YQITVGDEYT
451 VRGYNLRTSQ SGDSGVYLSN TLTVPVQFSL LGKQASVAPF VGADVGALKS
501 NHPDARTIRM AGLAAGVRFD LPYARMSFTY SKPVGAQPGG APRAPVWLYI
551 NAGLSF
```

C C^{195}-C^{224}

```
  1 QAQGSLLPGA RDLNRIDDRQ RKEQLQRDIE RALTRPPVEL NPQSEAAAPA
 51 RKPDATSGHT VTVHAVDLDF GVEGRLFDPA PLVQDYLNRP LDNEQLFLLV
101 KALSAALYDR GYATSIVTFV PPGVVDGVLK LKVEWGRIKG WLIDGKPLEG
151 TRDRMMVFSA MPGWQDKVLN VFDIDQAIYN INNGGKTGNI TIVPAI C GY
201 SYLDLQLQRR ALPRVSLGMD NSGPC PENG RYKYNASVTA NDLLGLNDTL
251 GLYIGNRYYR DAGHDAERNY DLMYSVPLGR TRLDLQTGYS TYRNLLKTRY
301 GQYQSAGNSR SFGLKATRLL YRDTRSQFSV YGGLKLRQNK NYLAGTRLDV
351 SSKHYSDVTV GMQYSTQRGA NAYFGDLSFT RGVGVNNGKY AAYDERGPQG
401 NVSRFNGSLA WTRYMALAGQ PIQWASQLGF QYSRQQLLNS YQITVGDEYT
451 VRGYNLRTSQ SGDSGVYLSN TLTVPVQFSL LGKQASVAPF VGADVGALKS
501 NHPDARTIRM AGLAAGVRFD LPYARMSFTY SKPVGAQPGG APRAPVWLYI
551 NAGLSF
```

D

```
  1 QAQGSLLPGA RDLNRIDDRQ RKEQLQRDIE RALTRPPVEL NPQSEAAAPA
 51 RKPDATSGHT VTVHAVDLDF GVEGRLFDPA PLVQDYLNRP LDNEQLFLLV
101 KALSAALYDR GYATSIVTFV PPGVVDGVLK LKVEWGRIKG WLIDGKPLEG
151 TRDRMMVFSA MPGWQDKVLN VFDIDQAIYN INNGGKTGNI TIVPAI C GY
201 SYLDLQLQRR ALPRVSLGMD NSGPC PENG RYKYNASVTA NDLLGLNDTL
251 GLYIGNRYYR DAGHDAERNY DLMYSVPLGR TRLDLQTGYS TYRNLLKTRY
301 GQYQSAGNSR SFGLKATRLL YRDTRSQFSV YGGLKLRQNK NYLAGTRLDV
351 SSKHYSDVTV GMQYSTQRGA NAYFGDLSFT RGVGVNNGKY AAYDERGPQG
401 NVSRFNGSLA WTRYMALAGQ PIQWASQLGF QYSRQQLLNS YQITVGDEYT
451 VRGYNLRTSQ SGDSGVYLSN TLTVPVQFSL LGKQASVAPF VGADVGALKS
501 NHPDARTIRM AGLAAGVRFD LPYARMSFTY SKPVGAQPGG APRAPVWLYI
551 NAGLSF
```

Figure 2 Supplement 1. Peptide mapping analysis of FhaC$^{C48-C224}$ and FhaC$^{C195-C224}$. Residues in red represent sequence coverage with (A,C) or without (B,D) reduction and alkylation. In the latter cases, the regions that contain the Cys residues were not characterized, suggesting the presence of an intramolecular S-S bond in both variants. Note that the sequences shown here contain an N-proximal Gly-Ser insertion for cloning purposes that has no effect on the structure or the activity of FhaC. The numbering of FhaC throughout the text corresponds to that of the native protein without this insertion.
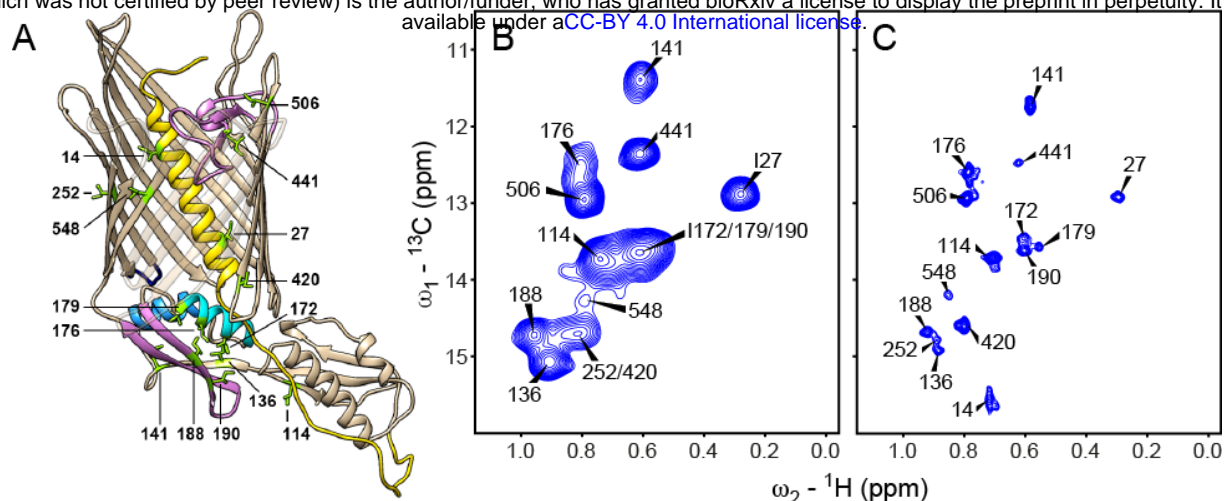
Figure 3. NMR analysis of Ile δ₁ methyl labeled FhaC in lipid bilayers. (A) Structure of FhaC with Ile residues labeled and drawn as green sticks. Color code of structural elements is as in Fig. 1. β-strands 1 to 4 are drawn transparently for visibility. (B) Methyl region of a solid-state dipolar hCH ^{13}C-^{1}H correlation spectrum of u-(^{2}H, ^{15}N), Ile-δ₁(^{13}CH₃)-labeled wt FhaC in *E. coli* polar lipid liposomes, recorded at 50 kHz MAS on an 800 MHz spectrometer. (C) Same region as in (B) of a solution-state heteronuclear multiple quantum coherence (HMQC) ^{13}C-^{1}H correlation spectrum of FhaC^{195R1} (same isotope labeling as in (B)) in ^{2}H-MSP1D1 nanodiscs containing deuterated DMPC and DMPG lipids, recorded on a 900 MHz spectrometer. The MTSL tag (called R1, see below) on residue 195 was reduced with ascorbic acid; peak positions are identical to those of wt FhaC in nanodiscs. These analyses were complemented by analyses of through-space correlations (Supplement 1) and relaxation dispersion experiments (Supplement 2).
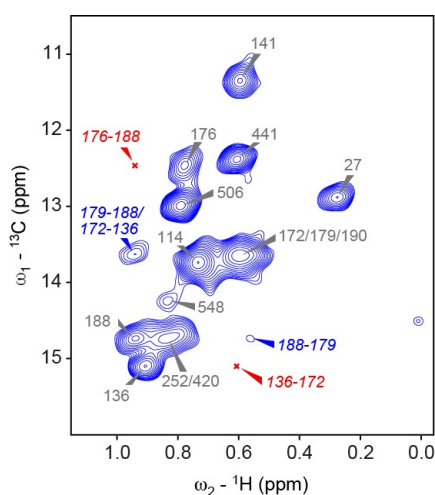
Figure 3 Supplement 1. NMR analysis of through-space contacts between Ile δ₁ methyl groups in FhaC in liposomes. 2D hChH correlation spectrum with 6.4 ms RFDR (Bennett et al., 1992) ^{1}H-^{1}H mixing of FhaC u-(^{2}H, ^{15}N), Ile-δ₁(^{13}CH₃) in d₅₄-DMPC/d₅₄-DMPG liposomes, recorded on an 800 MHz NMR spectrometer, to visualize through-space correlations between Ile δ₁ methyl groups close in space. Among expected inter-residue cross-peaks (^{1}H-^{1}H distance below 6 Å), peaks present in the spectrum are indicated in blue, those which are absent in red.
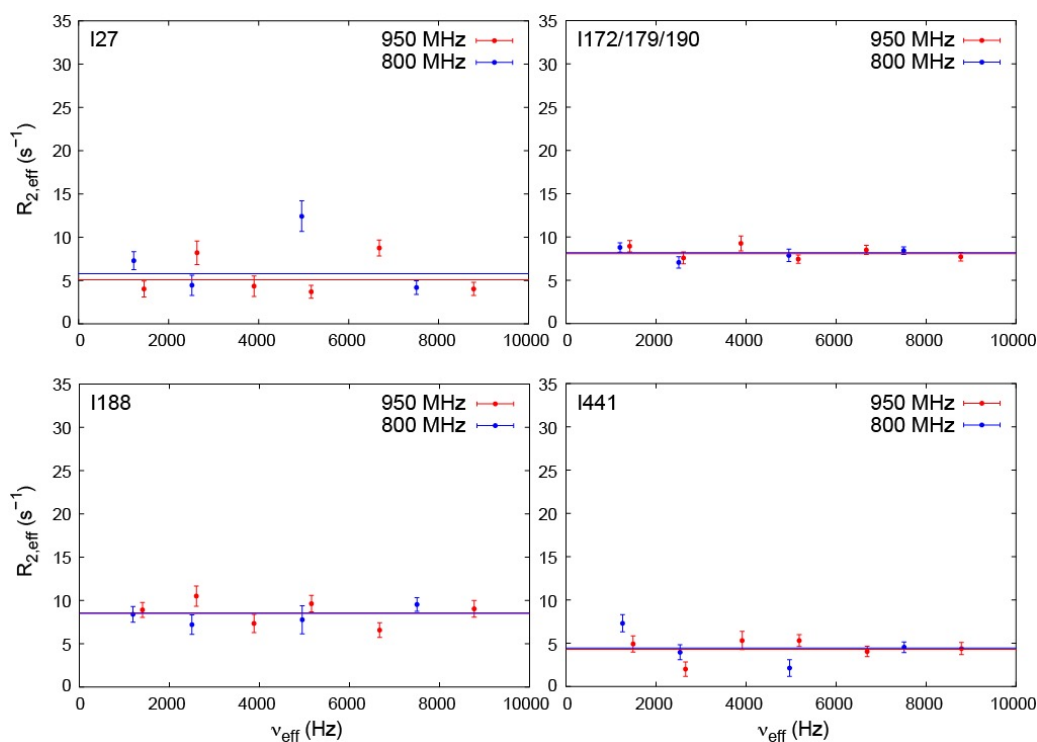
Figure 3 Supplement 2. NMR relaxation dispersion experiments to measure µs time scale exchange dynamics in FhaC. Effective ^{13}C transverse relaxation rates $R_{2,\text{eff}}$ extracted from solid-state NMR $R_{1\rho}$ relaxation dispersion experiments (Lewandowski et al., 2011; Ma et al., 2014) on selected Ile-δ_1 methyl groups of u-(^{2}H, ^{15}N), Ile-δ_1(^{13}CH$_3$)-labeled wt FhaC, recorded on 800 (blue) and 950 MHz (red) spectrometers at 50 kHz MAS frequency and 17°C sample temperature. Horizontal lines are best fits to the data using a model of no exchange (i.e. constant $R_{2,\text{eff}}$ values for varying applied B_1 radiofrequency fields and thus varying effective fields ν_{eff}). Models assuming exchange do not fit the data significantly better according to F test statistics or Akaike's information criterion (AIC) in any of the Ile-δ_1(^{13}CH$_3$) groups of FhaC. Notably, data from residue Ile[548] in strand β16, at the barrel junction with strand β1, could not be reliably analyzed due to low signal-to-noise.
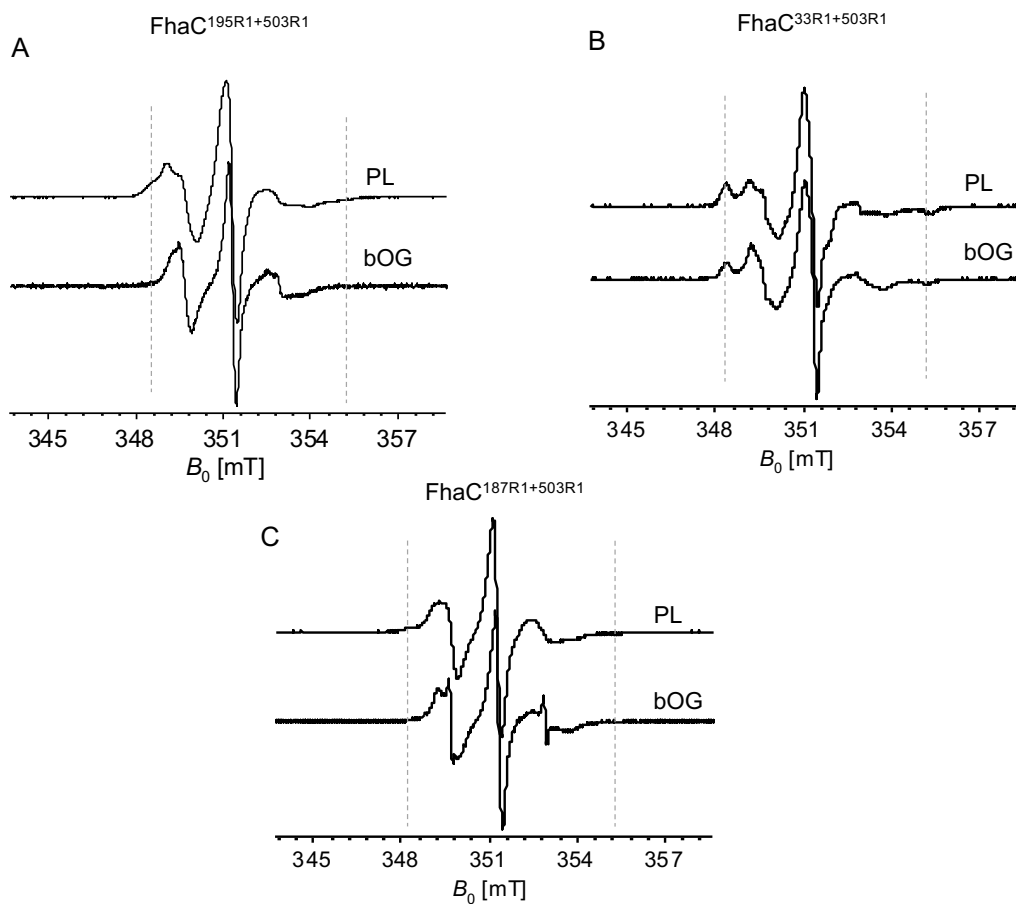
Figure 4. CW-EPR analyses of FhaC variants. (A) CW-EPR spectra of FhaC[195R1+503R1], (B) FhaC[33R1+503R1] and (C) FhaC[187R1+503R1] in bOG micelles and proteoliposomes (PL) made of *E. coli* polar lipids, respectively. The line shapes of the spectra result from different components. The outer splitting varies from 7.0 to 3.0 mT, and an intermediate component with a broadening of 5.0 mT is also observed. The dotted lines indicate the highest value of A_{zz} (hyperfine coupling) for the nitroxide spin probe between the unpaired electron and the nitrogen nucleus. Spectra obtained in various other lipid environments are found in Supplement 1.
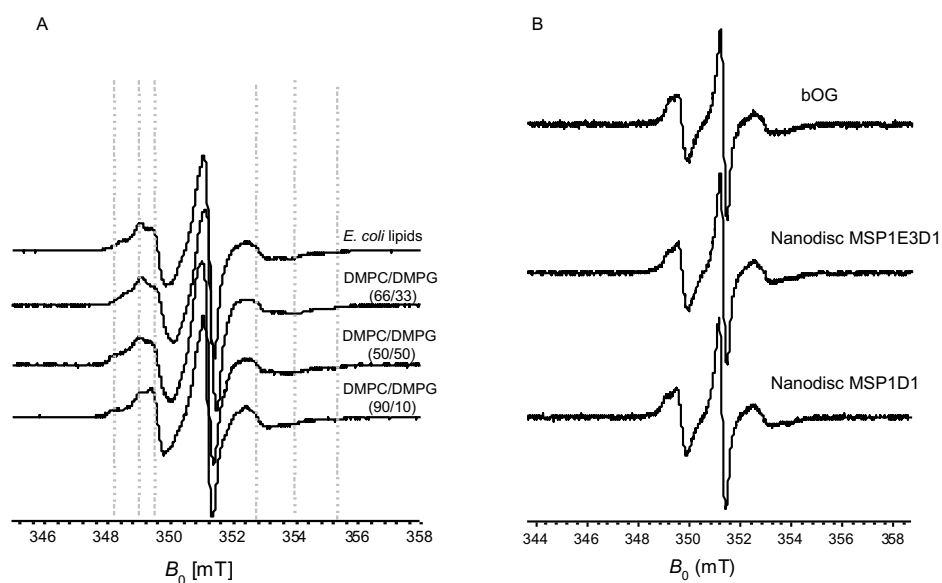
Figure 4 Supplement 1. CW-EPR spectra of FhaC[195R1+503R1] in various environments. (A) Proteoliposomes were made of DMPC and DMPG at different ratios, and the spectra obtained were compared with that of the same protein in proteoliposomes made of *E. coli* polar lipids. The dotted lines indicate the highest value of A_{zz} ($\Delta B = 7$ mT) for the nitroxide spin probe between the unpaired electron and the nitrogen nucleus, as well as two additional components on the EPR spectra related to two species with different mobilities. At DMPC:DMPG ratios of 66:33 and 50:50, the spectra are very similar to that in *E. coli* polar lipids. (B) FhaC was inserted in nanodiscs of two different sizes, made with MSP1D1 or MSP1E3D1, and a 66:33 ratio of DMPC:DMPG.
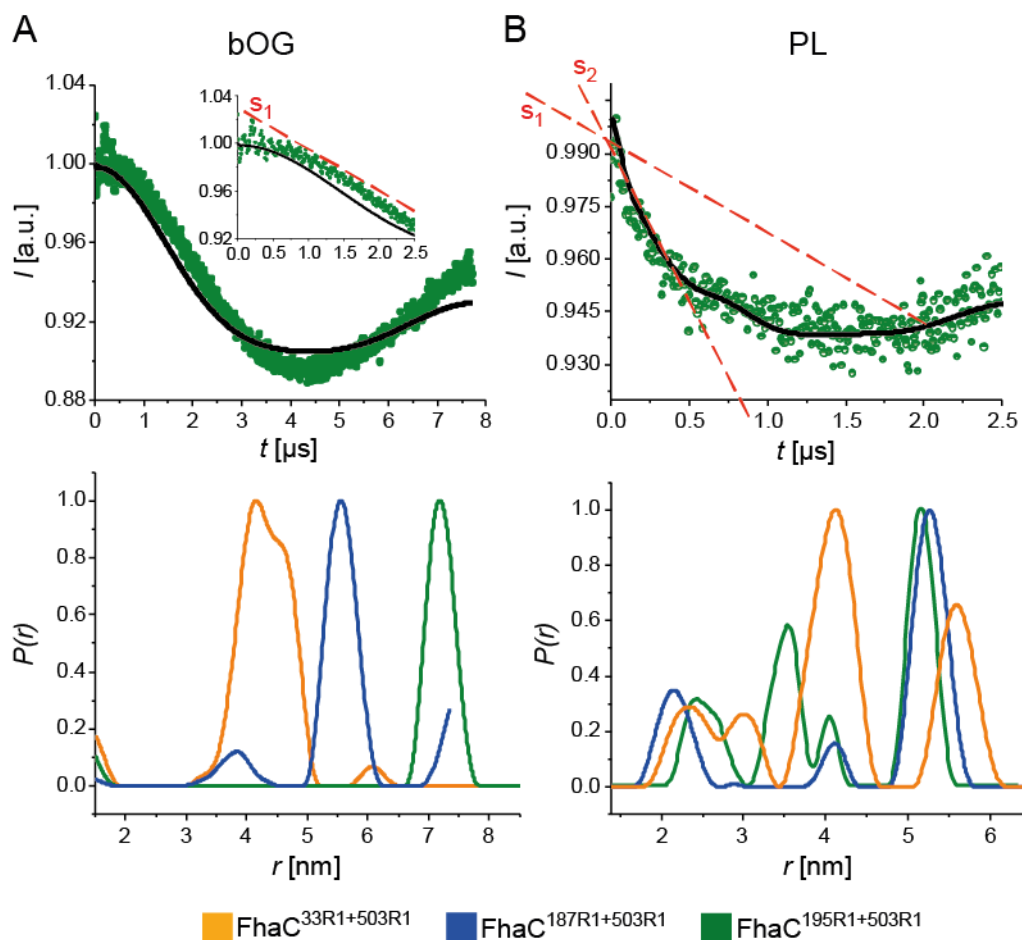
Figure 5. **PELDOR analyses of FhaC**. Dipolar evolution function for FhaC[195R1+503R1] (top), and distance distributions obtained by Tikhonov regularization of the dipolar evolution functions (bottom) for FhaC[33R1+503R1](orange), FhaC[187R1+503R1] (blue), and FhaC[195R1+503R1] (green) in bOG (A) and in proteoliposomes (B) prepared with *E. coli* polar lipids (PL). The black lines in the upper panels correspond to the fitting of the experimental PELDOR traces. The inset in A represents the first 2.5 µs of the dipolar evolution function for comparison with that shown in (B). The red dashed lines denoted S1 and S2 show the slopes of the first parts of the curves representing the dipolar evolution functions. Predicted distance distributions can be found in Supplement 1. Note that the longest distances measured depend on the dipolar evolution time *t*. As the lipid environment decreases the *t* that can be applied, the longest distances shift to smaller values for FhaC in proteoliposomes compared to bOG (Supplement 2). A mutation that severs the connection of the loop L6 to the inner barrel wall affects the EPR spectra of FhaC[195R1+503R1] (Supplement 3).
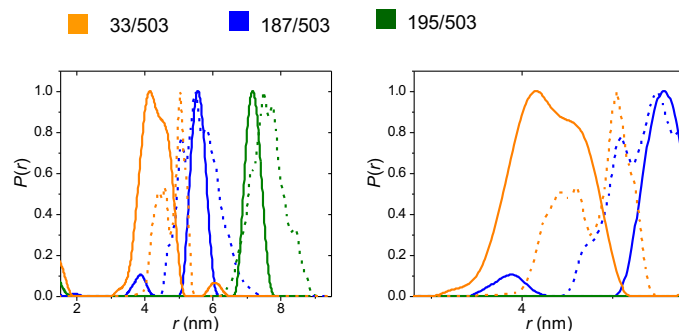
Figure 5 Supplement 1. Distance distributions from PELDOR experiments. The distance distributions obtained for FhaC[33R1+503R1] (orange), FhaC[187R1+503R1] (blue) and FhaC[195R1+503R1] (green) in bOG (solid lines) are compared with those predicted using a pre-computed rotamer library of the MTSL spin probe attached to specific residues on the PDB structure of FhaC (dashed lines) (Jeschke, 2020). In the right panel, a zoom on the 3-5 nm region shows the broad distribution for FhaC[33R1+503R1].
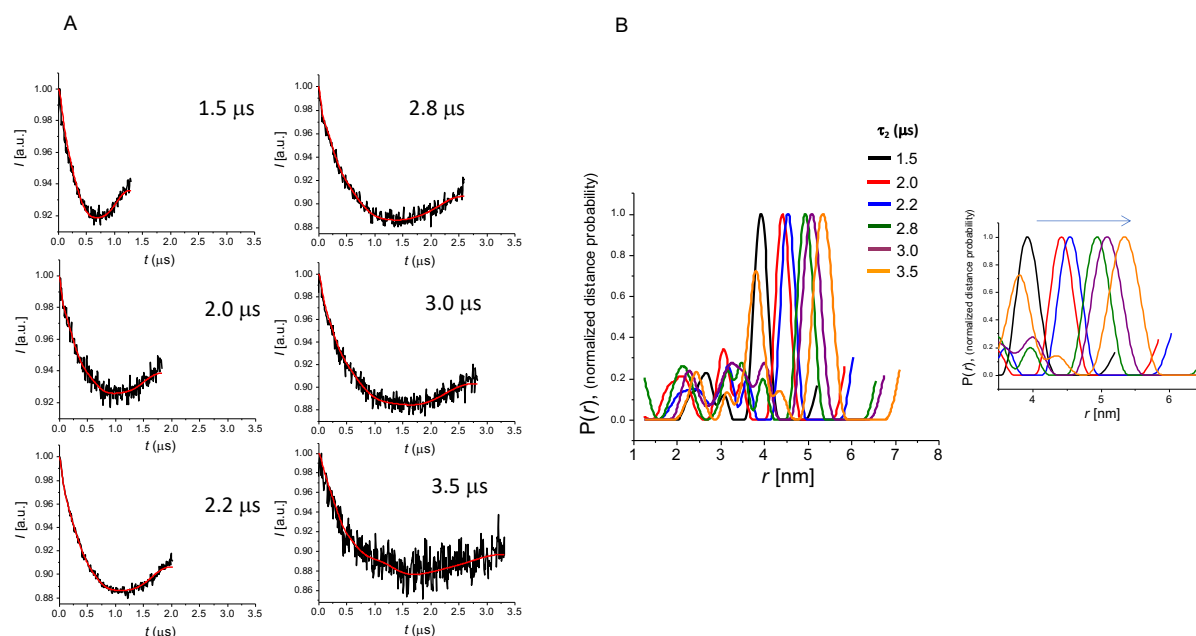
Figure 5 Supplement 2. Dipolar evolution signals recorded with different delays τ_2 and corresponding distance distributions. FhaC[195R1+503R1] in *E. coli* lipids liposomes was used in this experiment. (A) The dipolar evolution signals were measured at increasing dipolar evolution times *t*. (B) The longest distance measured shifts to longer values for longer dipolar evolution times *t* since long, but not short distances are sensitive to the value used in PELDOR experiments. The lipid environment decreases the dipolar evolution time that can be applied, which results in an apparent shift to smaller distance distribution values. The right panel is a zoom on the 4-6 nm region.
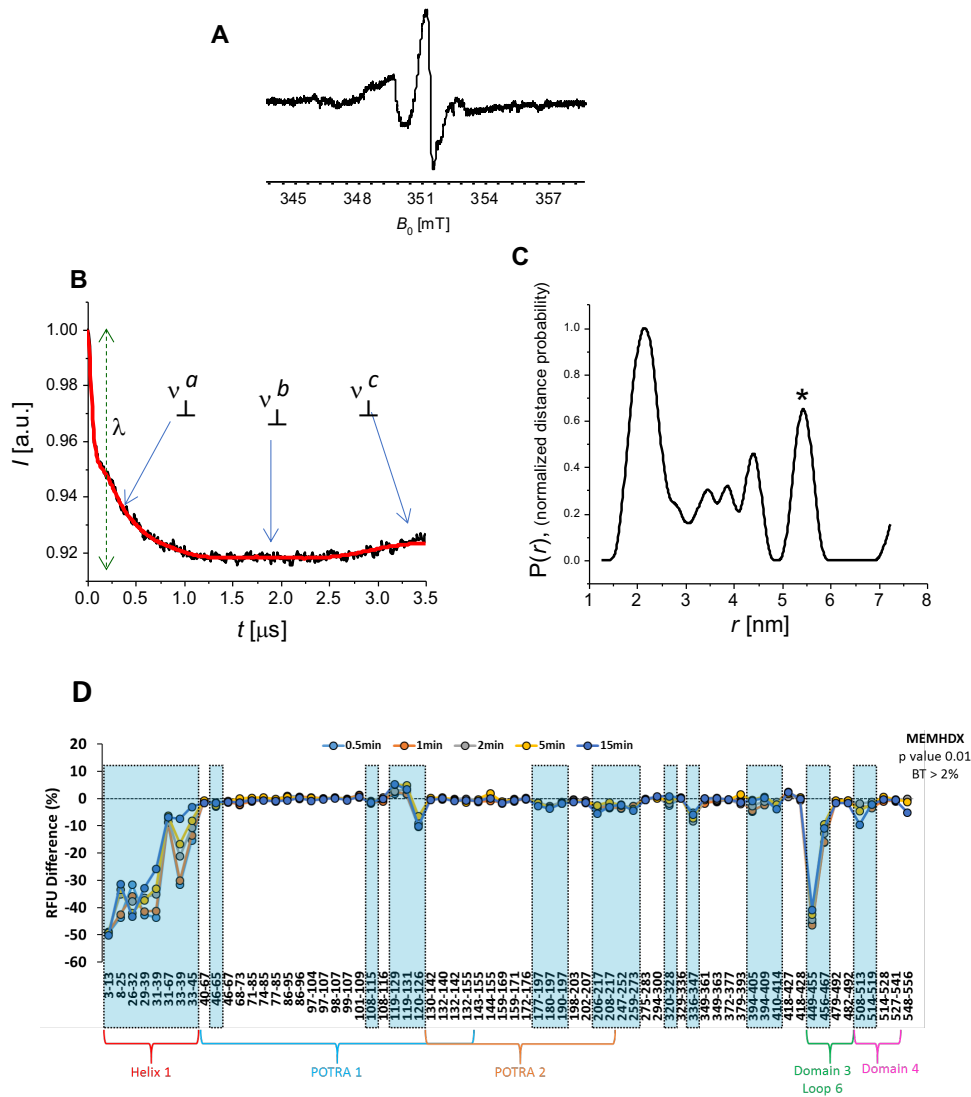
Figure 5 Supplement 3. Effect of the L6-barrel interaction on conformational changes of FhaC. (A) CW-EPR spectrum of FhaC$^{R492+195R1+503R1}$ in proteoliposomes. (B) Dipolar evolution function for the PELDOR signal. (C) Distance distribution obtained by Tikhonov regularization of the signal depicted in (B). The asterisk corresponds to the longest distance measurable as a function of the t parameter applicable in this experiment. (D) Results of hydrogen-deuterium exchange mass spectrometry. Comparison of relative fractional deuterium uptakes (RFU) between wt FhaC and the FhaC^{R492} variant. Negative values correspond to less deuterium uptake by the wt protein relative to FhaC^{R492}.
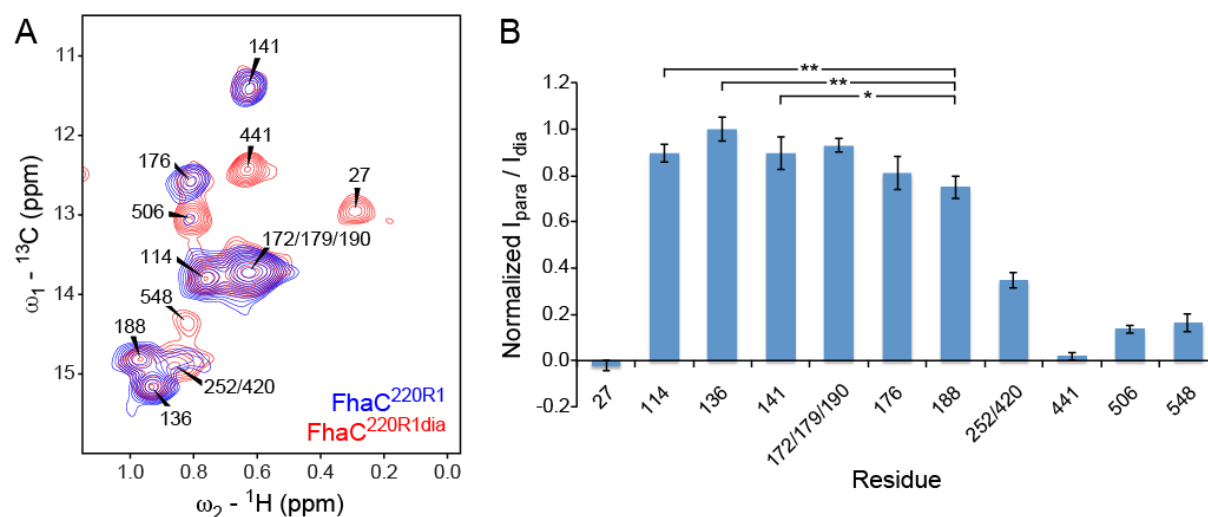
Figure 6. NMR paramagnetic relaxation enhancement experiments (PRE) on FhaC. (A) Superposition of dipolar solid-state hCH ^{13}C-^{1}H correlation spectra of u-(^{2}H, ^{15}N), Ile-δ_1(^{13}CH$_3$)-labeled FhaC samples in *E. coli* polar lipid liposomes, with a paramagnetic MTSL tag (FhaC^{220R1}, blue) or with a diamagnetic MTSL analog (FhaC^{220R1dia}, red) attached to the introduced Cys^{220} residue. Spectra were recorded at 800 MHz ^{1}H Larmor frequency. (B) Ratios I_{para}/I_{dia} of Ile-δ1 methyl peak intensities in the hCH correlation spectra of FhaC^{220R1} and FhaC^{220R1dia} shown in (A), normalized to the maximum ratio observed in Ile^{136}. Error bars are calculated based on spectral noise levels. * and ** indicate significant ($p < 0.05$ and $p < 0.01$, respectively) attenuation of the Ile^{188} signal relative to the signals of the reference residues Ile^{114}, Ile^{136}, and Ile^{141}. Distances between the probe and the Ile residues are shown in Supplement Table 1. PRE experiments in nanodiscs (Supplement 2) complement these analyses.

Ile residue	Avg. dist. to paramag. center (Å)
14	7.1
252	11.7
548	16.5
27	17.5
441	18.6
506	25.3
420	32.0
179	32.1
176	34.1
188	35.4
141	38.4
172	40.4
136	42.0
190	43.5
114	56.6

Figure 6 Supplement Table S1. Estimated Ile $C\delta_1$ – MTSL distances in the crystal structure conformation of FhaC[220R1]. Shown are distances (in Å) between Ile $C\delta_1$ nuclei and the estimated average position of the paramagnetic center in FhaC with a MTSL spin label on residue 220 (FhaC[220R1]). An ensemble of 200 MTSL conformations compatible with labeling on FhaC residue 220 was calculated using the mtsslSuite web server (Hagelueken et al., 2012; Hagelueken et al., 2015) (http://www.mtsslsuite.isb.ukbonn.de/) and the FhaC crystal structure (PDB 4QKY). The average position of the paramagnetic center (taken as halfway between nitrogen and oxygen atoms of the MTSL nitroxide ring) was calculated from the coordinates of these 200 conformations; distances from that position to Ile $C\delta_1$ nuclei were calculated using PyMOL (The PyMOL Molecular Graphics System. Schrödinger, LLC). A horizontal line in the table indicates the distance from the paramagnetic center up to which attenuation effects on the NMR resonance of the corresponding Ile residue are expected if FhaC assumes a conformation as in the crystal structure.
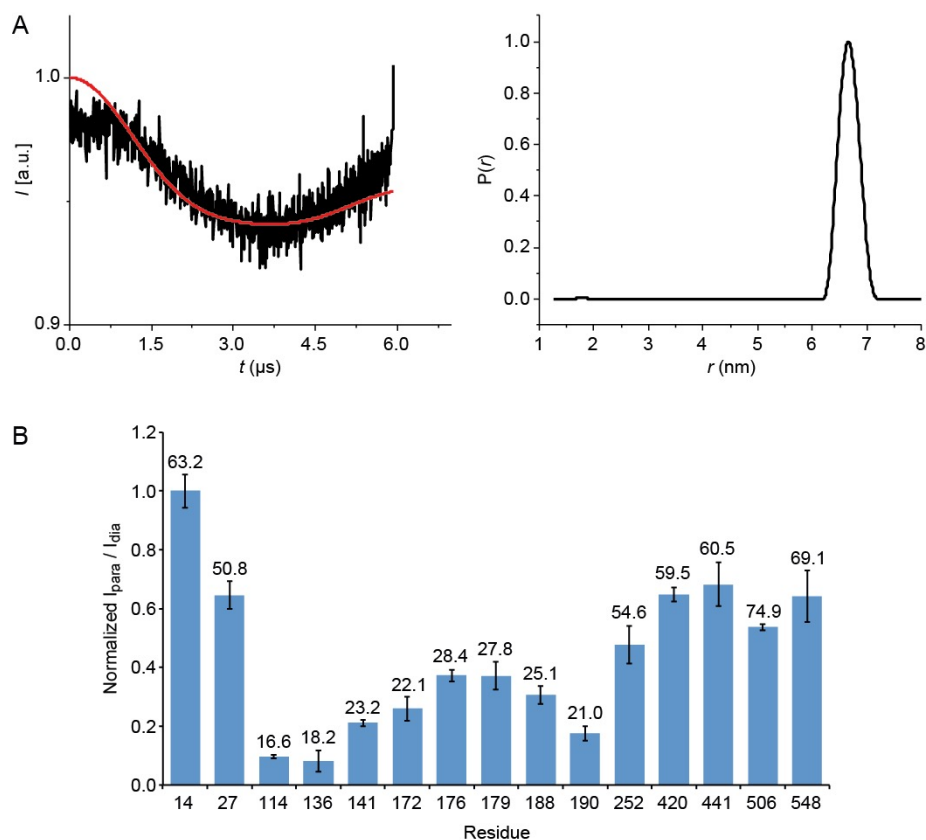
Figure 6 Supplement 2. Spectroscopic analyses of FhaC in nanodiscs. (A) Dipolar evolution function (*left*) and Tikhonov regularization (*right*) of the PELDOR signal of FhaC[195R1+503R1] in nanodiscs. (B) NMR paramagnetic relaxation enhancement experiments on FhaC[195R1] in nanodiscs. Ratios I_{para}/I_{dia} of paramagnetic vs. diamagnetic FhaC[195R1] Ile-δ_1 methyl peak intensities (normalized to their maximum value found for Ile[14]) extracted from ^{13}C-^{1}H heteronuclear multiple-quantum coherence (HMQC) experiments in solution before and after reduction of the MTSL spin label by addition of a 10-fold molar excess of ascorbic acid. Spectra were recorded on a 900 MHz spectrometer. Error bars are calculated based on spectral noise levels. Numbers above the bars indicate the distance between the $C\delta_1$ nucleus of the corresponding Ile residue and the average position of the paramagnetic center in an ensemble of conformations of the MTSL tag attached to Cys[195] in the FhaC crystal structure, calculated using the MtsslWizard PyMOL plugin (Hagelueken et al., 2012). Relative levels of signal attenuation due to the MTSL tag are perfectly in line with the relative distances of the corresponding residues from the paramagnetic center modeled onto the FhaC crystal structure, suggesting that FhaC in nanodiscs does not populate alternative conformations.
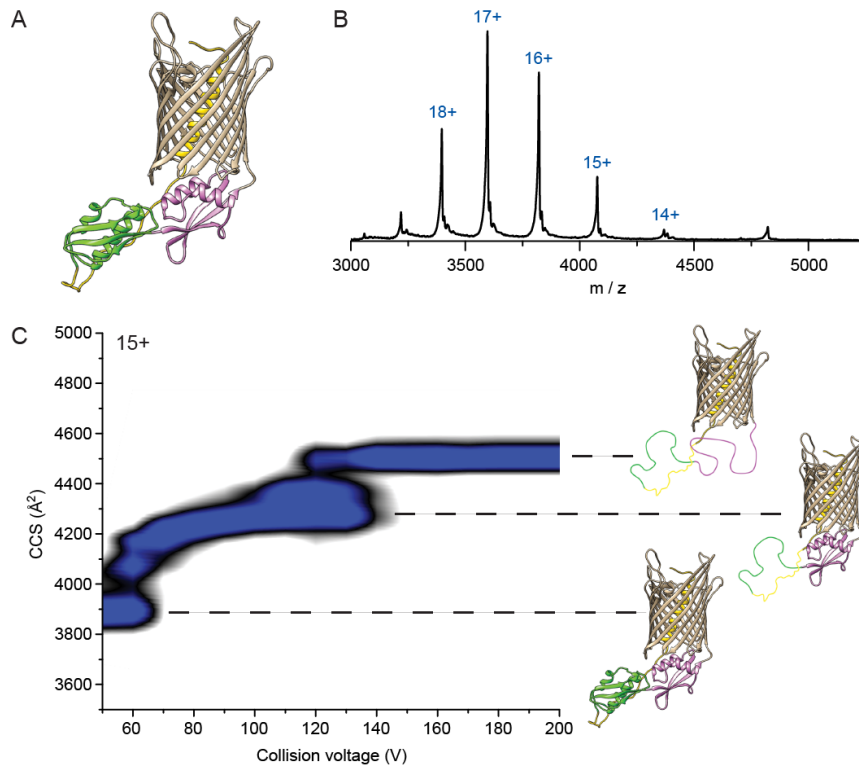
Figure 7. Native mass spectrometry analysis of WT FhaC. (A) Model of FhaC with H1 and the linker in yellow, and the POTRA domains 1 and 2 in pink and green, respectively. (B) Mass spectrum of WT FhaC released from its bOG micelle. The spectra at increasing collision energy are shown in Supplement 1. (C) Collision-induced unfolding (CIU) experiments show two dominant transitions that are likely linked to unfolding of the POTRA domains (see text), although the order in which they unfold is unknown. CIU profiles of control β-barrel proteins are shown in Supplement 2, and profiles of the FhaC$^{C4+C391}$ variant with H1 locked in the barrel are in Supplement 3.
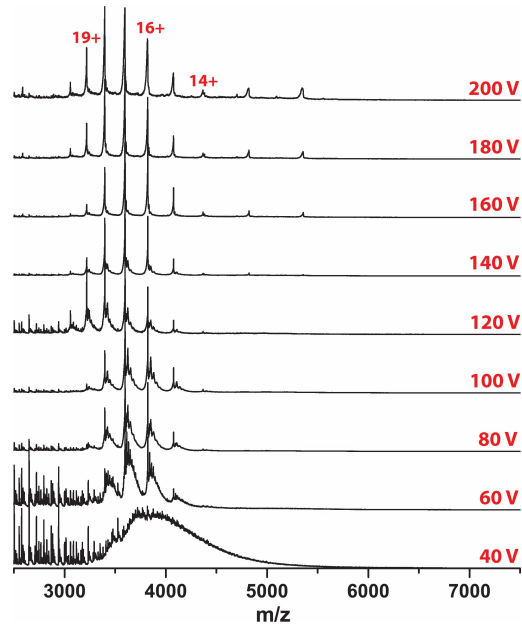
Figure 7 Supplement 1. Native MS analysis of FhaC in bOG micelles. The spectra were obtained at increasing collisional energy.
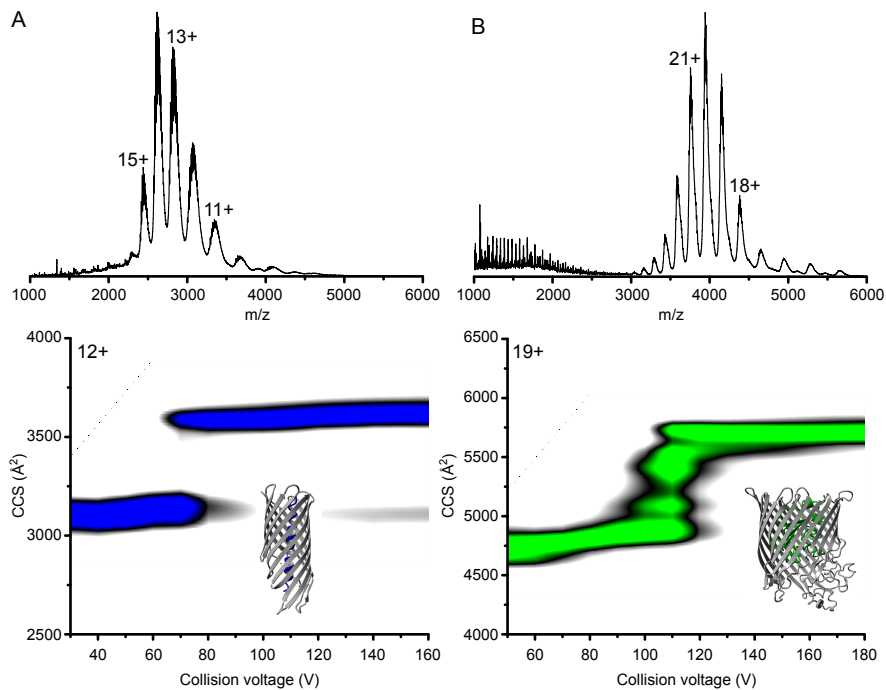
Figure 7 Supplement 2. Mass spectra and CIU plots of control OMPs. (A) SphB1-αβ is a truncated autotransporter (AT) containing only the β barrel with the preceding helical linker inserted in the barrel pore. (B) The TonB-dependent transporter BfrG is composed of a β barrel with a soluble N-terminal plug domain inserted in the barrel. The structural models shown are those of related transporters (PDB 1UYN and 3QLB, respectively), as the structures of SphB1-αβ and BfrG are not available. The mass spectra of the two OMPs released from their bOG micelles are shown at the top, and the CIU plots are below. Both show a single CIU transition, which suggests that the β barrels remain intact, while the soluble domains are ejected and unfold.
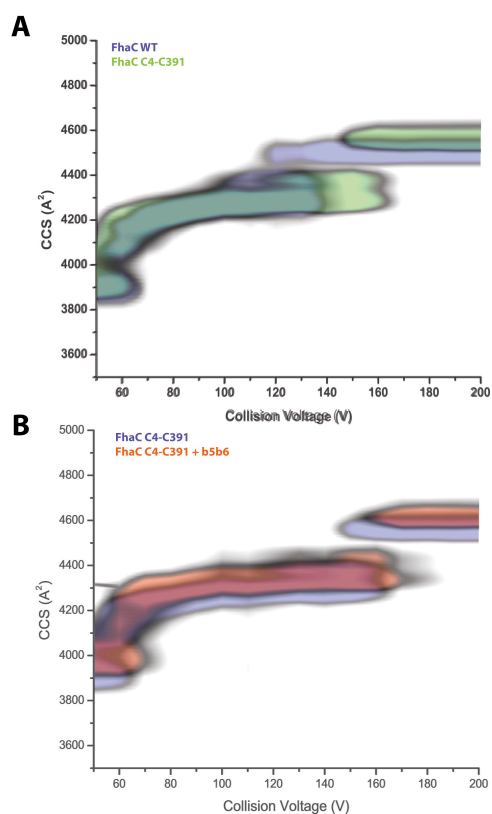
Figure 7 Supplement 3. CIU plots of FhaC$^{C4+C391}$. (A) Comparison of the CIU plots of wt FhaC (blue) and the FhaC$^{C4+C391}$ variant (green). (B) Overlay of the CIU plots of unbound FhaC$^{C4+C391}$ (blue) and FhaC$^{C4+C391}$ with the b5-b6 peptide bound (red). As for wt FhaC (see Figure 8), binding of the peptide to FhaC$^{C4+C391}$ increased CCS values at both low and high CE, suggesting that it induces enlargement of the β barrel, even with H1 inside.
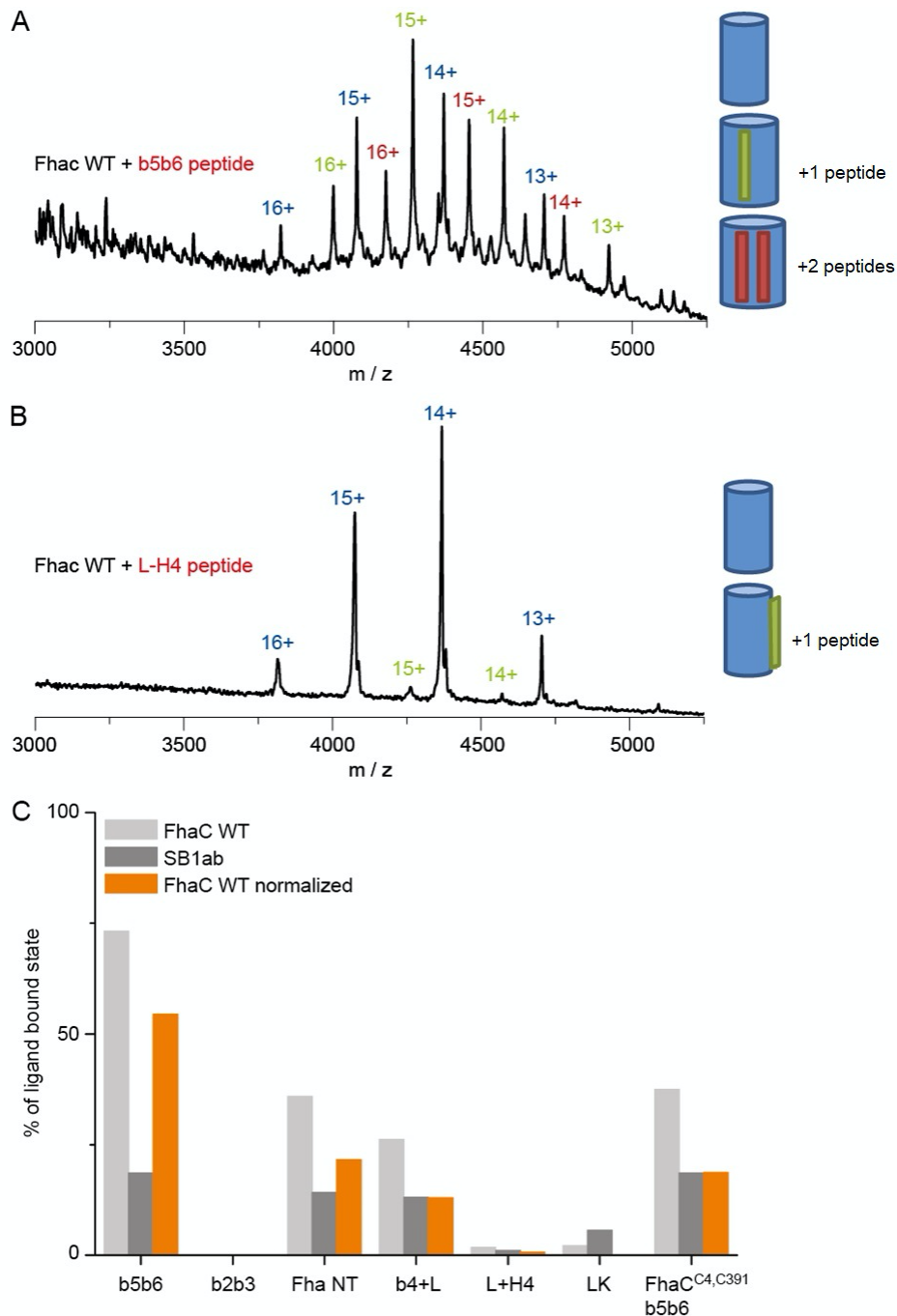
Figure 8. Binding of synthetic peptides to FhaC. (A) Mass spectrum of FhaC incubated with the b5-b6 peptide at a collisional energy of 150 V shows binding of the peptide to the protein under high-energy conditions. Schematic representations of the barrel with bound peptides are shown at the right. (B) Under similar conditions, little binding was detected for the L-H4 peptide. (C) Quantification of the binding of synthetic peptides to FhaC (light grey) and to the control β-barrel protein SphB1-αβ (SB1ab, dark grey; used to correct for non-specific binding). Orange bars show normalized values. The peptides used in this study are shown in Supplement 1.
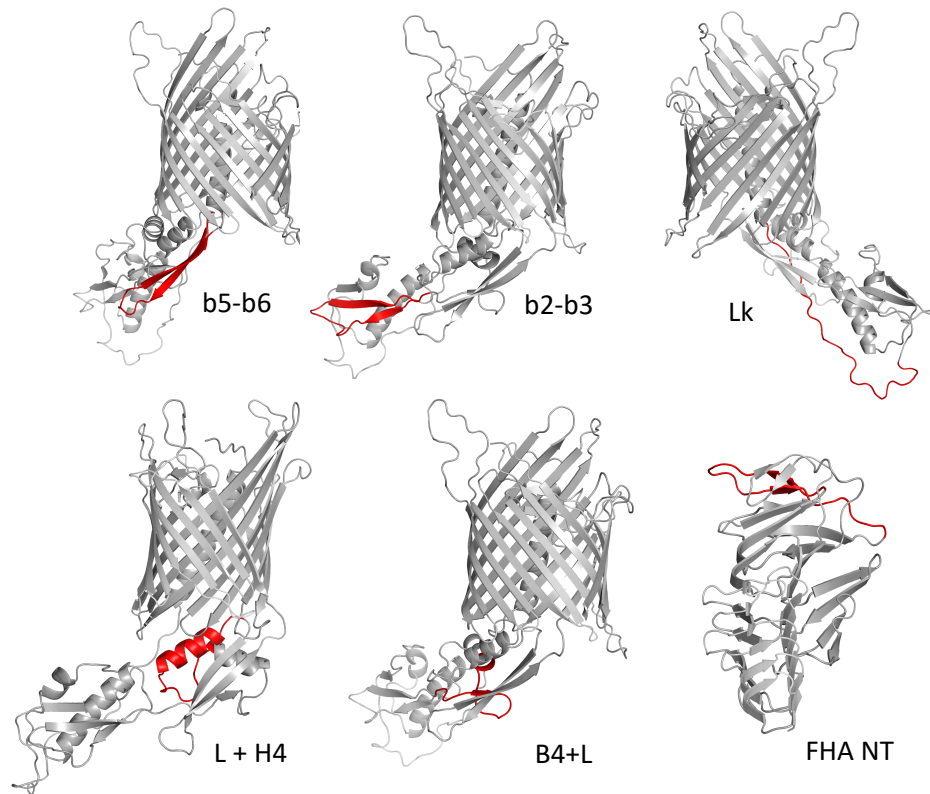
Figure 8 Supplement 1. Synthetic peptides used in this study. The first 5 peptides are shown in red on the structural model of FhaC, and the last one on the structural model of the N-terminal portion of FhaB (PDB 1RWR). The b5-b6 peptide (GKTGNITIVPADEYGYSYLDLQLQR) corresponds to the last two β strands of the POTRA2 domain that form an amphipathic β hairpin immediately preceding B1, the first strand of the β barrel. The b2-b3 peptide (SIVTFVPPGVVDGVLKLKVEWGR) encompasses the last two β strands of the POTRA1 domain. The Lk peptide (RPPVELNPQSEAAAPARKPDATSGH) corresponds to the linker between the H1 helix and the POTRA1 domain. The L+H4 peptide (AMPGWQDKVLNVFDIDQAIYNINNG) encompasses the loop (extended) region that precedes the H4 α helix and the H4 helix of the POTRA2 domain. The B4+L peptide (RIKGWLIDGKPLEGTRDR) corresponds to the β strand b4 of the POTRA2 domain followed by a loop region. Finally, the FHA-NT peptide (QTQVLQGGNKVPVVNIADPNS) corresponds to the N-terminal β strands b2 and b3 of FhaB forming a short hairpin, preceded and followed by loop regions.
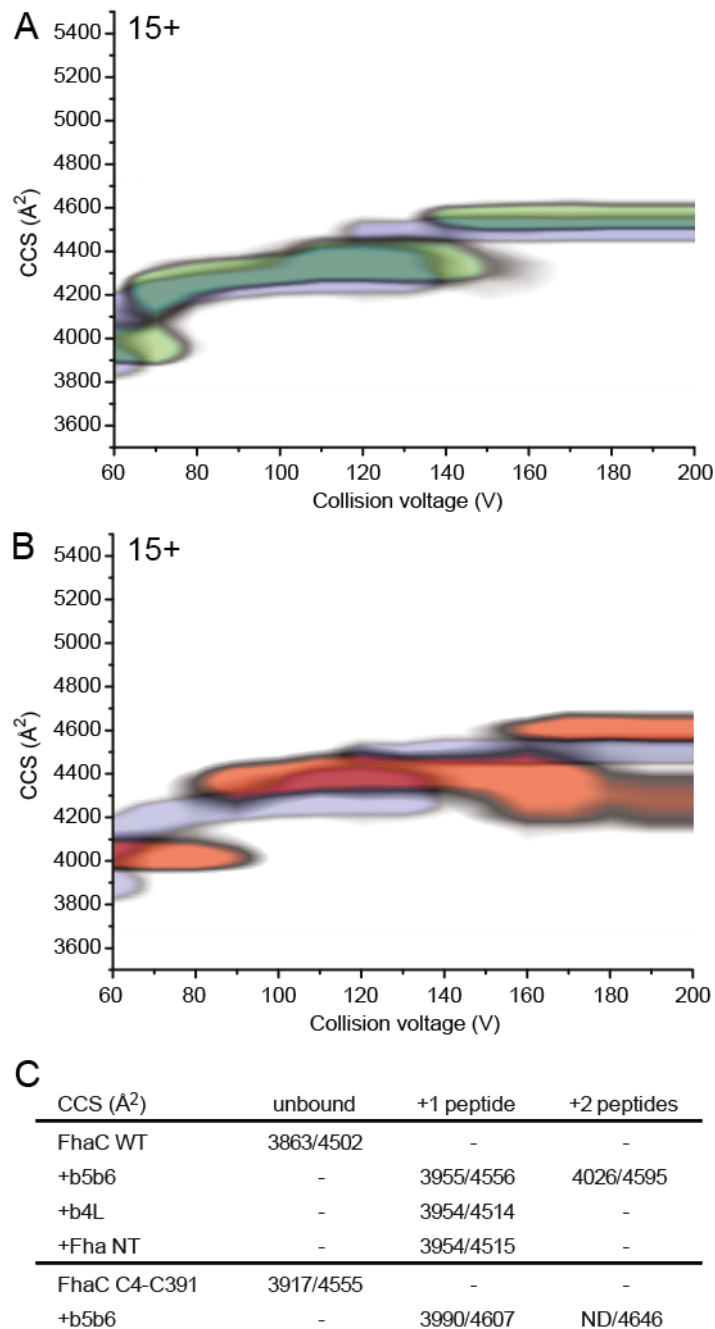
Figure 9. Collision-induced unfolding of FhaC with bound b5-b6 peptide. (A) Overlay of the CIU plots of FhaC with (green) and without (blue) one b5-b6 peptide bound. Increased CCS values are observed both under native conditions (low CE) and conditions in which the POTRA domains are most likely unfolded (high CE). (B) Comparison of the CIU plots of unbound FhaC (blue) and FhaC with two b5-b6 peptides bound (orange), which shows an additional CCS increase compared to FhaC with a single peptide bound. (C) CCS of FhaC with various peptides determined at low and high CE (listed before and after the slash). The measured values indicate that only b5-b6 enlarges FhaC in both conditions. The CIU plots of wt FhaC with the b4L and FhaNT peptides are shown in Supplement 1. The CIU plot of FhaC$^{C4+C391}$ with the b5-b6 peptide are shown in Figure 7 Supplement 3.
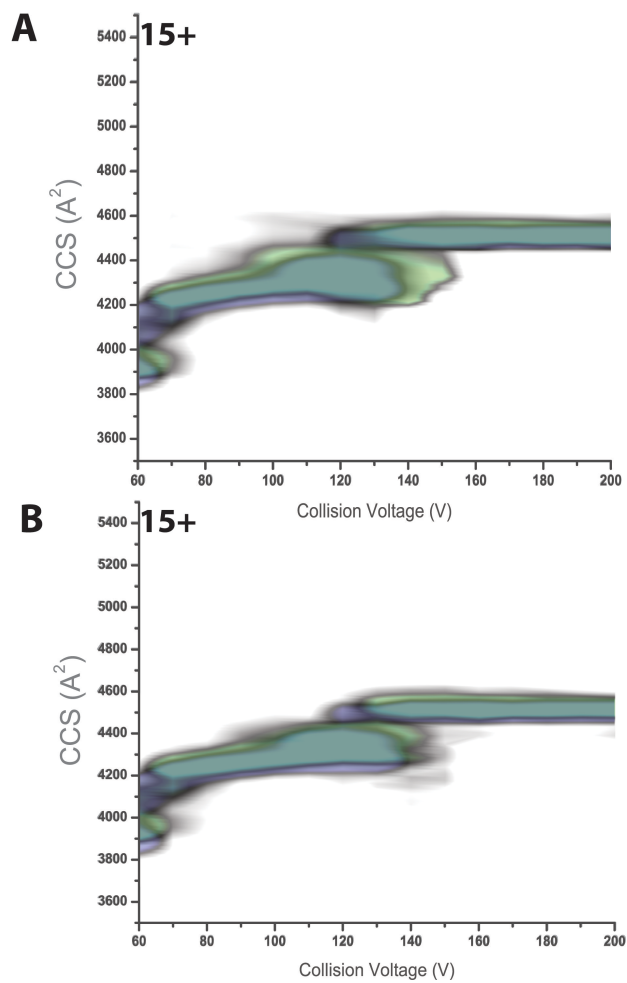
Figure 9 Supplement 1. CIU plots of FhaC incubated with synthetic peptides. (A) FhaC without (blue) or with (green) the FHA-NT peptide. (B) FhaC without (blue) or with (green) the B4+L peptide. In both cases the presence of the peptide causes an increased CCS at low collision voltage, but not at elevated collisional activation.